CO Diffusion in Layered Water Ices

Trish Nicole Lauck
Chesterfield, Virginia

Bachelor of Science, University of Mary Washington, May, 2008

A Thesis Presented to the Graduate Faculty
of the University of Virginia
in Candidacy for the Degree of
Master of Science

Department of Chemistry

University of Virginia
May, 2014

Eric Herbst

Ian Harrison

Karin Öberg

Abstract

The mobility of molecules in ice mantles on interstellar dust grains regulates the ice chemistry, and therefore much of the overall chemical evolution during star formation. Interstellar ices are typically dominated by water, followed by CO and CO_2. This study aims to quantify the rate and barrier for CO diffusing into water ice and a water:CO_2 ice mixture at low temperatures (15-23K), by measuring the mixing rate of CO and water in initially layered ices maintained at a constant temperature. The mixing fraction of CO as a function of time is determined by monitoring the infrared CO stretching band. Mixing is observed at all investigated temperatures on minute to hour time scales. The mixing rate and final mixing fraction depends on ice temperature, porosity, thickness and composition. Under the assumption that mixing is due to CO diffusion, the temperature dependence of the experiments are used to calculate the CO diffusion barrier to 100–200 K, significantly lower than the value used in current astrochemical models. Fick's diffusion equation is then applied to determine an analytic solution to CO diffusion in water ice and discuss the implications for our understanding of diffusion in ices more generally as well as the astrochemical implications.

Acknowledgements

First, I would like to thank my parents, family, and Andrew for their constant support in all my endeavors. My graduate school experience had its ups and downs, and they were always there for me.

With regards to my research, there have been many people that have helped me along the way. I am grateful to have worked with a skilled mentor and colleague, Mahesh; my experience designing and building the vacuum chamber with him was exciting and a wonderful opportunity. Our collaborators, Katie, LJ, and Herma were generous with their contributions to the work. Conversations with Eric, Ian, and John about topics here and there helped me make sense of my science, and I appreciate their guidance. Most importantly, there is Karin. I am glad that, as a new professor, she took a chance on me as one of her first students. She has been a kind, understanding and patient adviser. Not only did she impress me as such a successful woman in science, but she is an all-around good person who strives for greatness, and she inspires me to do the same.

I also want to acknowledge my Grad Council and science outreach families, including peers and administrators; being involved in the organizations allowed me to harness my leadership and service skills again, and to get to know so many people from across departments and the community.

Lastly, my friends, who have helped keep me sane at times, from both Chemistry and Astronomy, have been such a special part of my life in Charlottesville. We have shared many great times together and I look forward to many more.

Table of contents

Chapter 1

Introduction and background

Astrochemistry, in general, is the study of chemical processes in the interstellar medium. Understanding the chemistry that is happening can provide information about the physical conditions of an object in space. Also, studying the early stages of chemical evolution provides insight to the origins of life. In order to paint the full picture of what has been learned, the astrochemistry discipline relies on the interplay between three components: observations, experiments and theory. Observations allow us to measure the presence and abundances of molecules that are present in space. Theoretical models, in effort to reproduce observed values, predict the chemistry that happens, and provide hints of species or to search for with future observations. Laboratory experimentation is used to help understand observations by providing energy barriers and reaction rates that can be entered into the astrochemical models. With the three branches constantly working in together, the astrochemical field is trying to answer the many unanswered questions about the details of chemical evolution.

From an overall perspective, chemical evolution within the interstellar medium is tied to the stellar life cycle. The cycle both begins and ends with stellar death when gas and dust are emitted and spread out from old stars. This material starts to

condense to form a diffuse cloud, with gas densities of tens or hundreds particles cm^{-3} (predominately atomic and molecular hydrogen) and temperatures of 50 to 100 K. In the next phase, a portion of the cloud contracts further from up to 100 parcecs (where 1 parsec (pc) is about 3.3 lightyears) in size down to on the order of 1 pc, forming a dense molecular cloud, where star formation begins. With the exception of H_2 formation, most chemistry up until this point happens through exothermic ion-neutral reactions in the gas phase, with CO being a major product. At temperatures of 5-10 K and densities of 10^{3-4} cm^{-3}, dust grains, made of silicate or carbonaceous material, begin to become an important part of the chemical processing because molecules can form through collisions on the dust surface. As the central region of the cloud condenses further and radiation cannot escape, it becomes a protostar with its cold envelope and a central core, where the temperature increases to between 100 and 300 K. Chemistry becomes more interesting and rich in these regions; many larger organic molecules are observed (Herbst & van Dishoeck 2009). At the protostellar stage, as material from the outer envelope condenses inwards, it rotates around the core at an increasing rate causing a disk-like structure to form, and extra material is ejected away in outflows. As the extra material dissipates from the envelope after most of it is accreted onto not pre-main sequence star, dust and gas in the protoplanetary disk becomes dense enough to coagulate and form larger bodies. Eventually the disk evolves into a solar system with a central star and surrounding planets, until the star ages and the cycle begins again (Herbst & Yates 2013).

1.1 Interstellar ices

Chemistry in cloud cores and protostellar environments is of particular interest because those regions are at the very beginning stages of the star and planet formation

process, which goes hand-in-hand with the roots of chemical evolution. In the colder regions, i.e. prestellar cloud cores or protostellar envelopes, the dust grain surfaces are major reservoirs for molecules. At temperatures below 20 K many of the heavy elements and volatile species are frozen out in icy mantles formed on the grains, leaving only hydrogen and helium in the gas phase. The ices that build up on the dust particles have been directly observed in protostellar envelopes and cloud cores (Gibb et al. 2004; Öberg et al. 2011). Observations of interstellar ices show that the mantle composition is H_2O-dominated. CO_2 and CO are the next most abundant molecules, both at about $\sim$30% with respect to water, and there are trace detections of other molecules like methane, ammonia, and methanol. Most simple molecules, including water, CO_2, and methane, are formed through atomic diffusion and collisions that occur on the grain surfaces. An exception to this is the CO molecule, which accretes from the gas phase as a whole molecule onto the dust grains at temperatures below 20 K. Evidence has shown that in low density regions most of the CO participates in surface reactions to form CO_2, while at higher densities ($10^{5-7} cm^{-3}$) after a cloud has further condensed, the CO is depleted from the gas phase more quickly and builds up on the ice mantle (Garrod & Pauly 2011; Pontoppidan et al. 2008). Therefore, the ices formed on the grains have an amorphous bilayer nature, with water-rich, or polar, ices present in the inner ice phase of the mantle, and CO-rich, or apolar, ice in the outer phase; most of the CO_2 is found the water-rich ice environment (Pontoppidan et al. 2003, 2008). With this being only a very general depiction of the ice mantles, the details about the morphology and molecular diffusion within the mantle are unknown.

Since most of the molecular species are located on the dust grains, the ice mantles are important sites for chemical reactions. Many reactions are only efficient on the

dust grain surfaces, rather than in the gas phase because the surface can absorb excess energy that may be given off during the formation process. Atomic addition reactions are quite important surface processes that result in molecular formation. They occur when readily mobile atoms, i.e. hydrogen, diffuse along the grain surface and find another atom or molecule; this is a prominent method of water formation (van Dishoeck et al. 2013). Together with the availability of species present in the ice, the ability for the reactants to move about the mantle regulates the chemistry that occurs. In addition, diffusion can determine if volatile molecules, like CO, become trapped inside the ice matrix and therefore remain available for reactions even after its normal sublimation temperature of $\sim$20 K. In this case, chemical processes involving those volatile reactants would be possible at later stages into the protostellar collapse.

Complex molecules, with 6 or more atoms, are also formed through subsequent processes involving the simple starting molecules in the ices. Hydrogenation of CO, via atomic addition reactions on the ice surface results in CH_3OH formation(Herbst & van Dishoeck 2009). Methanol is an important precursor to larger organic molecules that can form through further processing on the ice mantles. Although it is difficult to detect larger, more complex species in the solid phase, there is evidence that they are indeed forming on interstellar ices. Astrochemical models have shown that there are efficient complex molecule formation mechanisms, e.g. for methyl formate, via surface reactions on ices that result in reasonable abundances (Garrod & Herbst 2006). In addition, recent radio observations of prestellar cores and protostellar envelopes (Öberg et al. submitted; Bacmann et al. 2012; Öberg et al. 2010), reveal the presence of complex organic species like CH_3CHO, $HCOOCH_3$, and CH_3OCH_3 in the gas phase, indicating that the molecules are formed in the ices and then released by some non-thermal process like photodesorption, for instance. Because the formation of complex

organic species can be traced back to CO and other simple molecules, it is essential to investigate the details about how they behave in ice mantles.

1.2 Interstellar and laboratory ice comparison

The behavior and movement of species within ices depends on the structure and composition of the mantle. It is well known that interstellar ices are amorphous, without an ordered structure, but the details of the morphology are still actively studied. Observations of the water band from infrared observations of ices in cold interstellar regions are consistent with laboratory spectra of high density amorphous solid water (Jenniskens & Blake 1994). Because water is formed through surface processes on dust grains, the nature of the water ice matrix that results is not considered to be very porous (Garrod 2013b). Also, with the typical oxygen abundance in molecular clouds being 5×10^{-4} with respect to hydrogen, the upper limit for the thickness of an ice mantle is on the order of a hundred monolayers, if most of the oxygen is used in water formation (van Dishoeck et al. 2013). Recent simulations by Garrod (2013b) have shown that the structure of the forming water mantle can vary with different accreting gas densities and temperatures. A cold pre- or protostellar environment exhibits gas densities typically on the order of 10^{6-7} molecules cm^{-3}, and the infalling material spends roughly 10^5 years at a temperature below 25 K, according to Pontoppidan et al. (2008). These astrophysical conditions and timescales, of course, can not be directly reproduced in the terrestrial laboratory, but useful information from experiments can be correlated to the processes that occur in interstellar ices.

Astrochemically relevant ice experiments in the laboratory are designed to investigate a particular process that is applicable to ices found in space. With the best ultra high vacuum conditions, pressures of 10^{-10-11} Torr are achieved, which corre-

sponds to about 10^8 molecules cm^{-3}. The residual gas in a typical ultra high vacuum chamber is dominated by H_2, similar to the targeted interstellar conditions, but the density is an order of magnitude higher. Using cryogenic sample cooling systems, sample surfaces can be cooled to lower than 10 K, but the gas or vapors used to build ices are introduced into the chamber at temperatures much higher than the sample, in many cases at room temperature. These environmental conditions within the chamber are some of the equipment limitations that are faced in the laboratory. Other limitations come into play when choosing the conditions for growing ice films on a sample substrate.

Several factors can affect the morphology of a laboratory ice film that make it either more or less representative of an interstellar ice analog. When studying a process that occurs when the bare dust grain surface is exposed (before it is coated with ice), the sample substrate material choice is important; one would likely choose a silicate or carbon-based substrate, e.g. (Katz et al. 1999; Sabri et al. 2014). If the targeted process happens within the bulk of the ice, the substrate is less of a factor because the grain surface sites do not play a part, and the sample substrate usually chosen to aide in the efficiency of the ice analysis, e.g. a transparent crystal, for instance. A key difference in laboratory ices when compared to interstellar ices is the porosity. In the case of water, pure layers, when deposited as whole water molecules in the laboratory, are not directly representative of the mantles that form in space, since water there is formed by surface reactions of hydrogen and oxygen. Simulations of interstellar water ice formation and growth show that the ice has a relatively low porosity, compared with a mantle that is grown by whole-molecule accretion, with similar fluxes and random angles of incidence (Garrod 2013b). However, there is evidence that when water ice is deposited with a collimated molecular source at a

normal incidence angle, the porosity is quite low, and the porosity increases with increasing angle of incidence (Kimmel et al. 2001; Raut et al. 2007). The porous nature of amorphous laboratory ices allows for molecular movement in pathways that may not be available in interstellar ices.

The pores within amorphous water ices grown in the laboratory are vacant spaces that form during the deposition process. These empty pockets can be important sites for diffusion or trapping in laboratory studies. In the literature, a few types of pores with different sizes are described. Micropores are the inherent pores that form during deposition of both a diffuse gas and a collimated source with normal incidence. There is evidence that the micropores are thin in diameter, accommodating up to only a few molecules across (Raut et al. 2007), but the diffuse deposition yields greater microporosity with a different morphology than a collimated source. A larger pore type is called a mesopore that is formed when ices are deposited at an angle where shadowing effects of the columnar growth result in large voids up to tens of nm wide (Smith et al. 2011). Karssemeijer et al. (2014) describes the properties of another type of pore, a nanopore, which is a small (6 $\mathring{A}$), strong-binding well on the surface of a water matrix. The different sizes and characteristics of the pores provide several environments that affect diffusion of molecules within the ice mantle, and by studying these processes, information obtained can be correlated to the interstellar diffusion process.

1.3 Ice diffusion

In the general conceptualization of processes occurring within the icy mantles on dust particles, diffusion plays an important role, but the mobility of most species in ices is poorly understood. Reaction networks in astrochemical models currently incorpo-

rate estimated diffusion parameters for the movement of species on and within ice matrices. Current models use 30-80% of a desorption barrier as an estimation for the energy required for diffusion (Garrod & Pauly 2011; Garrod 2013a; Chang & Herbst 2012). The lower barrier estimations in these models are based on model trials with varied diffusion-to-desorption barrier ratios; which ever ratio input resulted in model abundances comparable to the observed values was the value chosen. Desorption barriers that are included in the models were derived from laboratory experiments that measured the binding energy of the species to the ice surface. Because the models only estimate the diffusion barriers based on the desorption barrier value, the current predictions are highly uncertain. Direct measurements of the diffusion behavior are needed in order to make the models more complete.

Not only the measured energy parameters of diffusion are lacking; the mechanisms of the diffusion processes are also not well understood. Molecules may have several pathways for movement in and on the ice surfaces. General concepts of bulk and surface diffusion have been discussed, but the details of the mechanisms are widely debated.

1. Surface diffusion

    (a) Diffusion along the outer surfaces of the ice mantle, those directly exposed to the gas environment is the simplest form of surface diffusion. Models treat the movement of molecules or atoms undergoing surface diffusion as hops from one surface site to another in a random-walk manner (e.g. Chang & Herbst 2012; Garrod 2013a), a process that depends on the number of sites available and the energy required to make a hop.

    (b) Within the ice matrix, the pores walls are analogous to an outer surface, and the diffusion process there is thought to be similar. However, depend-

ing on the structure of the pores, the mechanism may be more complicated if the pore size limits the available pathways.

(c) Both pore walls and outer surfaces can have nanopore sites, mentioned previously, that may involve a different surface diffusion mechanism in order to escape from that site, as opposed to the simple hopping route.

2. Bulk diffusion

(a) Bulk diffusion is described as movement of a molecule or atom within the inner matrix of an icy mantle. This process may involve molecule or atom swapping within the mantle (Öberg et al. 2009; Garrod 2013a). This concept would require the diffusing molecule to switch places with the matrix molecule, as a substitution event.

(b) Another theory is that a molecule diffusing through the bulk of a matrix moves into interstitial spaces between molecules (Chang & Herbst submitted).

The bulk diffusion process is thought to be more difficult, and therefore requiring more energy, than surface diffusion. Recent models from Garrod (2013a) and Chang & Herbst (submitted) use separate values for the diffusion of a species, corresponding to the two different processes, with the lower estimate described above as the surface diffusion barrier, and the bulk diffusion value being roughly double, under the simple assumption that a bulk molecule has twice the number of binding partners. These barriers are incorporated assuming the process occurs in a water dominated matrix, but there is likely an ensemble of barriers depending on the composition and morphology of the ice mantle.

1.4 Recent CO diffusion studies

To effectively investigate a molecular diffusion process, it is best to focus on one particular molecule at a time. The process of CO diffusion in water ice is a good place to start since interstellar ices are dominated by water, and CO is one of the most abundant species. Until recently, there has been a lack of quantitative information about the diffusion mechanism and energies required for CO diffusion in water ices; therefore, astrochemical models use estimated values (the lowest being 400 K (Garrod 2013a)) for the diffusion energy barrier, as fractions of the desorption barrier for CO, which is 1150 K or 100 meV. There have been a few recent laboratory experiments and theoretical simulations that target this process in order to obtain the necessary information.

In computational simulations, values for the diffusion parameters can be extracted by modeling a system that represents the targeted process. One of the first quantitative models for CO diffusion on water from Karssemeijer et al. (2012) simulated CO surface diffusion on three different crystalline water ice substrates. The model represents a single CO admolecule on a three bilayer water substrate. The average value reported for CO surface diffusion in the simulations with crystalline water was 575 K, or 50 meV. Recently the same group modeled the process on an amorphous water substrate. In that study, results indicated that there are two populations of CO with different mobility characteristics, one in strong nanopore bindings sites with a diffusion barrier of 80 meV, and the other in weaker surface sites with a barrier of 30 meV (Karssemeijer et al. 2014).

Different techniques and conditions have been used to perform quantitative laboratory studies of the CO diffusion process. The first set of results for CO diffusion in water were from experiments exploring segregation of CO in mixtures with wa-

ter. In this study from Öberg et al. (2009), the reported barrier for CO diffusion in an amorphous water matrix via segregation, detected by infrared spectroscopy, was 300±100 K, or 25 meV, and the mechanism described was a surface process via pore pathways. These experiments were performed under ultra high vacuum conditions with thin (10–32 ML) ices at temperatures ranging from 23 to 27 K. Other recent experiments measured CO diffusion by monitoring the desorption of CO from a layered sample, both under high vacuum conditions. Mispelaer et al. (2013) report a diffusion barrier of 10±15 meV for CO diffusing out of an ice film consisting of a pure layer of amorphous water on top of a layer of pure CO. Karssemeijer et al. (2014) report a value of 26±15 meV for the diffusion of CO out of a mixture of CO:H_2O layered underneath pure water. Both of these experiments consisted of layers with thicknesses >450 ML, and were performed at temperatures ranging from 32 to 50 K. They also conclude that the diffusion occurs by moving along pore surfaces. Even with the varying experimental conditions, these sets of experiments are similar in that the results are measurements of CO movement and diffusion out of the water matrix, either by segregation or desorption. Because of the complex and irregular water morphology in laboratory ices, diffusion out of the matrix most likely involves a combination of diffusion mechanisms that are perhaps reflected in the single barriers that were derived from each experiment.

1.5 This work

In the attempt to further constrain the process by which CO diffuses in an amorphous water matrix, a set of experiments were designed to measure CO as it mixes into a water layer. The focus of this study is to quantify the diffusion rate of CO into amorphous H_2O ice starting with a layered ice structure under a range of experimental

conditions, and based on these experiments derive an analytic CO diffusion function and diffusion barrier. Chapter 2 presents the new experimental set-up designed to explore the physics and chemistry of thin ices, and Chapter 3 describes the experimental procedures specific for this study. The experimentally measured CO:H_2O mixing rates as a function of temperature, ice thickness, ice morphology and composition are presented in Chapter 4, together with the modeling of these experiments to extract the diffusion rate and barrier for CO. The results are discussed in light of previous experimental and theoretical work, and astrochemical impact in Chapter 5. Chapter 6 offers a brief summary and a few concluding remarks, along with some ideas for future directions.

Chapter 2

Chamber Setup

The laboratory setup used for this work was the first chamber system built by the Öberg astrochemistry group; it was designed and assembled during the fall of 2012 through the summer of 2013. The chamber setup was specifically designed for interstellar ice analog experiments, with several custom instrumentation attachments, and room for additional future attachments.

2.1 Main chamber

The stainless steel ultra-high vacuum (UHV) chamber (custom-made, Pfeiffer Vacuum) can accommodate many attachments in different configurations because of the versatile port locations. The main body of the chamber is spherical in shape with an inner diameter of about 13 inches. Protruding from the main body are 18 ports with conflat flanges of varying sizes, as shown in Fig. 2.1. All ports, with the exception of ports 1 and 18, have a distance of 220mm from the center of the chamber to the outer edge of the flange opening. The edge of port 1 is 195 mm from the center, and the distance from the edge of port 18 is 300 mm. The volume of the main chamber is

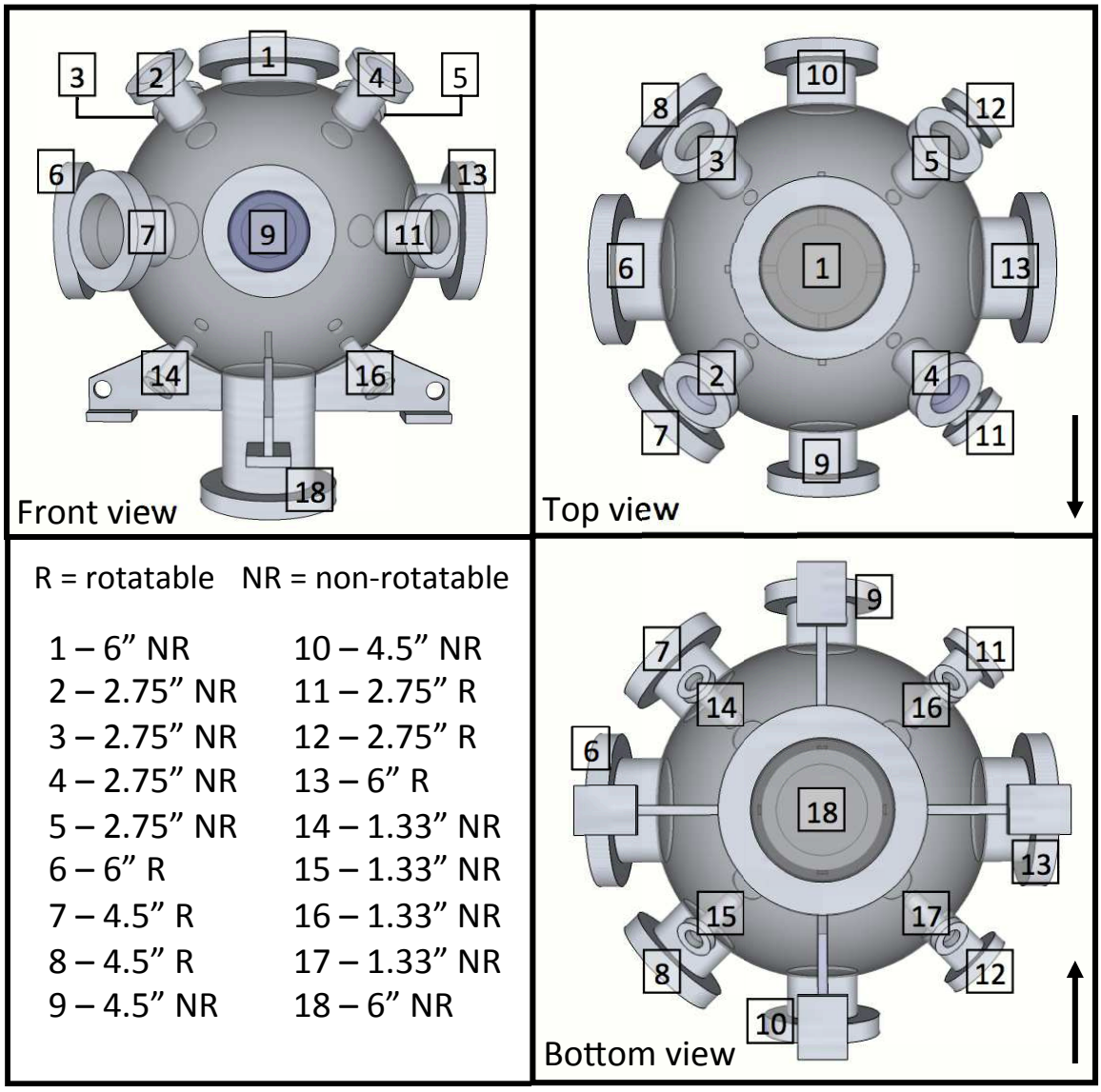

Fig. 2.1.— Three-dimensional drawing of the main chamber, showing front, top and bottom views. Each port is labeled with a corresponding number, and they will be referred by those numbers. The arrows in the top and bottom view panels indicated the direction of the front of the chamber.

21.1 L. Standard glass windows are attached at ports 2, 4, 9, and 10. Currently, ports 3, 12, 14, and 16 are not in use and are closed off with blank flanges, offering room for additional attachments in the future. When attaching equipment, windows, or blank flanges to the chamber, standard oxygen-free high-conductivity (OFHC) gaskets (Kurt J. Lesker Company), bolts, and nuts were used to seal the chamber port connections.

2.2 Chamber pumping mechanisms

To achieve UHV pressure levels, several pumps are used on the system. A Pfeiffer Turbo HiPace 400 pump with a pump speed of 400 L/s, is mounted to the bottom, port 18, of the chamber. The turbo pump is backed by a Pfeiffer DUO 10M rotary vane pump. The pressure of the chamber is monitored via various pressure gauges attached to the system. Baratron (0-1000 Torr) and pirani gauges are fixed to port 17 on the main chamber and on the line coming from the turbo pump to the rotary-vane pump, respectively. A cold cathode ionization pressure gauge (MKS 423-I-Mag) is mounted to port 5 of the chamber. All the gauges are connected to an MKS digital combination vacuum gauge controller (937B), where the pressure is continuously monitored. At room temperature (RT), the evacuated chamber base pressure, measured by the cold cathode gauge, is better than 1×10^{-9} Torr, even prior to a chamber bake-out, with H_2 as the dominant gas constituent, as indicated by mass spectrometer readings. UHV pressure obtained in the evacuated chamber with a cooled sample substrate reaches better than 3×10^{-10} Torr, due to cryopumping. When venting the chamber, a nitrogen gas line is attached to a variable leak valve, which is connected to port 15.

2.3 Temperature control

The experiments performed with this chamber setup are based on the ability for the sample substrate to be cooled down to temperatures low enough to grow ice films by depositing a gas into the chamber.

2.3.1 Sample substrate

The sample substrate used in the setup is a cesium iodide (CsI) crystal disk, that is 2 mm thick and 24 mm in diameter. CsI was chosen for the substrate material because it is infrared (IR) transparent from 42000 to 172 cm^{-1}, offering a wide range with no interference for IR spectroscopic studies, and it is a robust crystal under cryogenic conditions. From repeated observations on this system, KBr cracks at very low temperatures (<30 K), while CsI does not.

2.3.2 Variable temperature cryostat

The temperature of the sample substrate is controlled by the cryostat mechanism fixed at the top, port 1, of the chamber, with the cold tip extending down to the center of the chamber. The substrate is mounted between two silver (Ag) gaskets in the nickel plated copper sample holder at the end of the cryostat shaft, allowing for good thermal contact. The sample holder is an optical ring with a removable face piece that is fastened by small screws, and when assembled and holding the substrate, there is a 19 mm diameter clear view window. The holder is connected to the cold tip of a closed-cycle helium cryostat (Model CS204B, Advanced Research Systems, Inc.; compressor: ARS-4HW), capable of cooling the substrate down to 11K. The cryostat is mounted to the chamber via a differentially pumped (Pfeiffer, 60 L/s pump speed) UHV rotary seal (Thermionics RNN-400) that allows 360^o rotation of the substrate

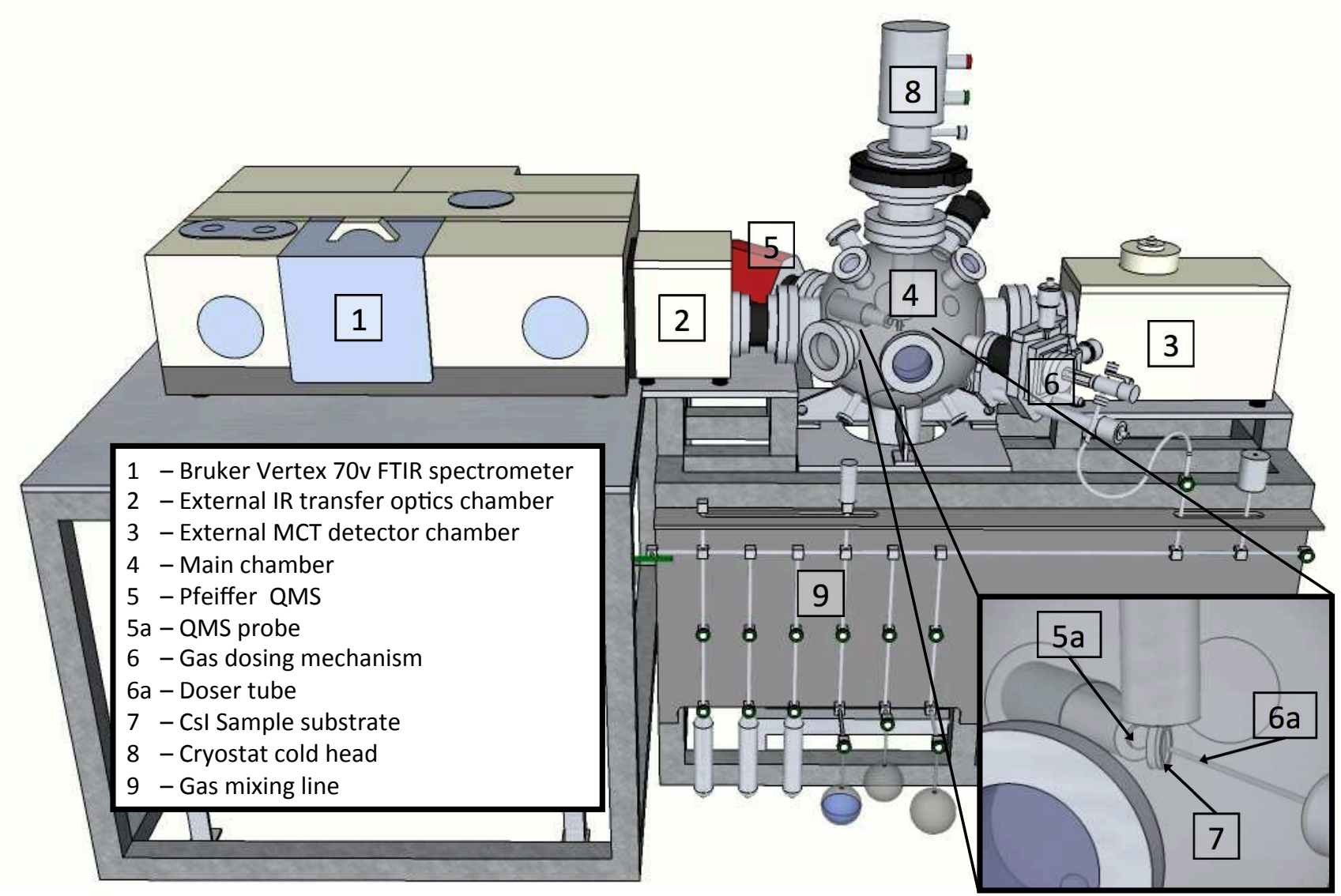

Fig. 2.2.— Three-dimensional view of the chamber, with the main experimental instrumentation marked.

window inside the chamber without breaking the vacuum during the experiment. Under the current configuration, the sample window is in 0^o position when it is facing port 11. A 50 ohm thermofoil heater is installed on the cryocooler tip so that the temperature of the substrate can be varied between 11-350 K. Temperature is controlled and monitored by a cryogenic temperature controller (LakeShore Model 335) using two calibrated silicon diode sensors (accuracy of 0.1 K), one connected directly to the sample holder and the other near the heating element.

2.4 Instrumentation

For the work presented in this thesis, infrared spectroscopy and mass spectrometry techniques were used during the experiments. The chamber also has capabilities for vacuum UV photon irradiation studies, but that was not used for this thesis.

2.4.1 Infrared spectroscopy

Infrared (IR) spectroscopy, in general, is used to measure the absorption features in the infrared that correspond to the frequencies of bond vibrations between the atoms in a molecule. These absorption features are used for identification also for quantification, since the intensities of the signals are directly correlated to the amount of species present. Used most commonly today, Fourier transform infrared (FTIR) technology is efficient and powerful because it measures all frequencies from the source simultaneously instead of having to scan each one individually, as in older methods. The instrument uses a beamsplitter that separates the source IR beam into two optical beams; one beam is reflected off of a fixed mirror, while the other reflects off of a mirror on a moving mechanism. The beams are recombined, but because the path lengths for the two beams are different, they interfere with each other, and the resulting

interferogram has the information for the entire frequency range embedded in the data as a function of the moving mirror position. The computer software quickly and easily performs the common Fourier transformation mathematical operation to extract the spectral information from the interferogram.

The instrument used in this setup is a Bruker Vertex 70v FTIR spectrometer with a liquid nitrogen cooled mercury cadmium telluride (MCT) detector. Manufactured as a standard instrument, the spectrometer is equipped with an internal sample compartment and detector. The IR beam from the spectrometer source enters and exits the UHV chamber through custom KBr windows located on either side of the chamber, attached to the ports 6 and 13. The IR beam exiting the spectrometer is initially focused onto the CsI substrate by the custom designed (Bruker) transfer optics located inside the external interferometer chamber consisting of a flat mirror and an off-axis paraboloidal mirror. The beam, after exiting the UHV chamber, is refocused onto the MCT detector using a similar optics assembly located inside the detector chamber. MCT detectors are commonly used for infrared spectroscopy. The semiconductor CdTe alloy has a band gap of 1.5 eV, while the semimetal HgTe alloy has no band gap; therefore, a mixture of mercury cadmium and telluride yields an alloy with a band gap within that range. This energy range is ideal for detecting infrared photons, which cause an electron to jump to the conduction band, and the electron detection is translated into a signal. To avoid thermal noise, the detector is cooled with liquid nitrogen during operation.

The spectrometer, the external interferometer chamber on the left side of the UHV chamber, as well as the MCT detector chamber on the right side of the main chamber are continuously evacuated down to less than 2 mbar. With evacuated instrument chambers, the interference from atmospheric water vapor or CO_2 is minimized and

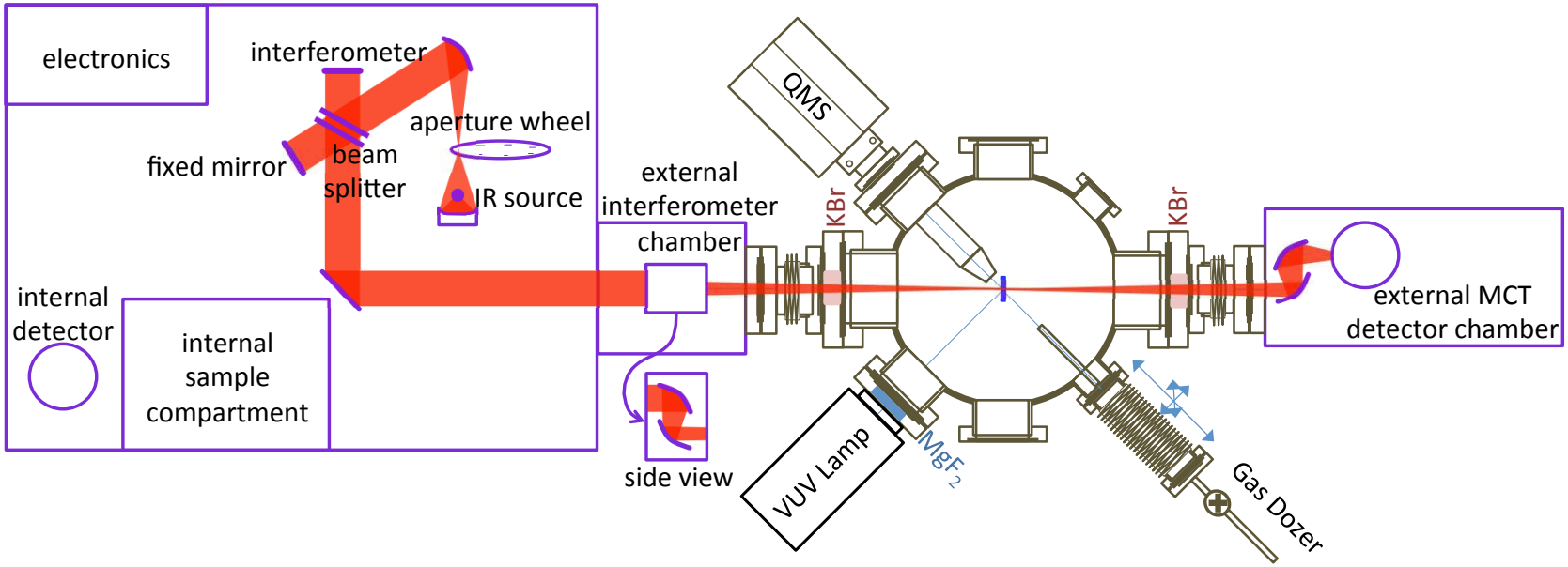

Fig. 2.3.— The path of the IR beam is shown in a top view schematic of the setup. Key instruments and chamber components are labeled. Figure modified from version by M. Rajappan.

weak spectral features are measurable.

The IR beam is optimal at apertures of 2.5 mm and less for sampling films on the CsI window. Quantifiable IR signals are detected at sample window angle positions of 0–90^o and 180–270^o. The infrared absorption of ices grown on the CsI substrate are measured in the transmission mode from 4000-400 cm^{-1}.

2.4.2 Mass spectrometry

To measure the gas inside the chamber, either the background or any species that have desorbed from the sample surface, mass spectrometry is used. A Pfeiffer Prisma Plus quadrupole mass spectrometer (QMG 220M1, mass range 1-100 amu) (QMS) with a minimum secondary electron multiplier (SEM) detection limit of 10^{-14} Torr and resolution of 0.5 amu is mounted on port 8 of the main chamber. In this position, the probe end of the QMS comes within 40 mm of the CsI substrate window. The sample window faces normal to the QMS probe when turned to a 180^o angle. Detection of desorbed species is optimized when the substrate is faced normal to the probe.

2.5 Gas mixing line and doser

Gases and mixtures are prepared in the custom designed gas mixing line, and they are delivered into the chamber via the doser. The gas line is independently pumped (Pfeiffer, 60 L/s pump speed), and the pressure of the gases in the line is monitored with two baratron gauges (1000 Torr and 20 Torr range). A pirani gauge is used to measure base pressure of the line to less than 5×10^{-4} Torr. Pure gases are stored in glass flasks or stainless steel canisters that are connected throughout the gas line. The line is designed with several on/off valves (SwageLok), one of which allows the gases to flow to the gas doser. Mounted at port 11, the gas doser consists of an xyz

stage, precision leak valve (MDC vacuum), and a deposition tube (4.8 mm diameter, 14 inches long) directed normal to the CsI surface face when at 0^o angle position. The precision leak valve allows for a controlled flow of gas into the chamber. Using the control knobs on the xyz stage, the deposition tube can be positioned in the z-direction at distances between 0 and 90mm from the substrate window, and minor adjustments can be made in the x- and y-directions to center the position. The long deposition tube creates a nearly-collimated molecular beam of gas molecules during deposition.

Chapter 3

Methods and Procedures

3.1 Gas sample and mixture preparation

3.1.1 Reagents

Deionized water (H_2O)

Deuterated water (D_2O), 99.9%, Cambridge Isotope Laboratory, Inc.

Carbon monoxide gas (CO), >99%, GT & S, Inc.

Carbon dioxide gas (CO_2), >99%, Isotec

The water and deuterated water samples were further purified by three freeze-thaw cycles under vacuum.

3.1.2 Gas sample handling

When preparing gases for an experiment, the mixing line was kept at $\sim 70^o$ C with heating tapes to minimize condensation of less volatile gases and vapors in the line. The line was evacuated to the base pressure prior to introducing a gas species into the main gas line, and also often times the line was flushed two or three times with

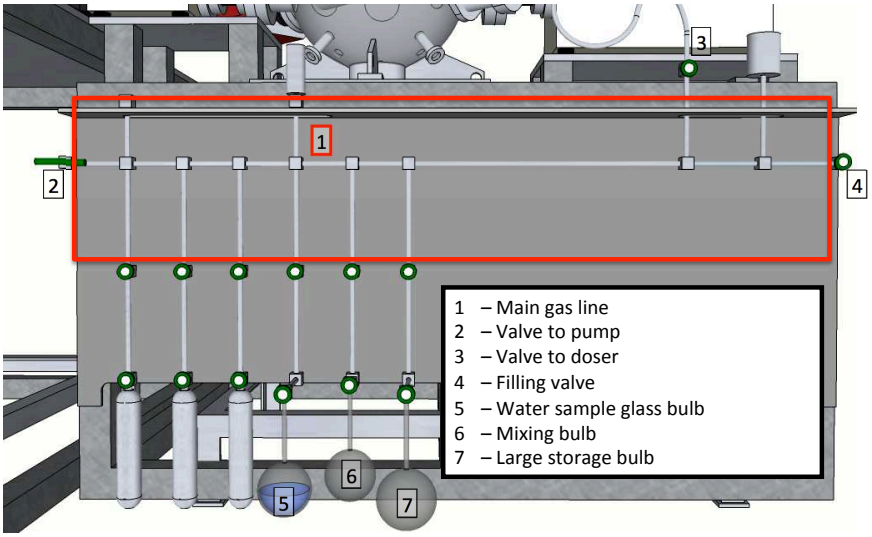

Fig. 3.1.— Close up of the gas line, with important features indicated. The portion of the main gas line used for mixture and sample preparation is boxed in red.

the gas to minimize contamination. Pure gas samples and pre-made mixtures were introduced into the main line to a pressure of 10 Torr in preparation for deposition.

3.1.3 Mixing procedure

The isolated main gas line section, shown in figure 3.1, was used to maintain a constant volume segment of the line for the mixing process. Starting with the condensable gas, water vapor from the vessel was allowed to fill the section, and then closed off again to measure the pressure in the section of the line. Then, the valves to the evacuated mixing bulb were opened, and, using liquid nitrogen under the vessel, the vapor was condensed into the bulb. This process was repeated until the desired amount by partial pressure of vapor of the water was in the mixing bulb. The valves to the mixing bulb were closed, and the vessel was brought to room temperature. Then, in main section of the gas line (evacuated and flushed with the second species), the desired amount, by partial pressure ratio, of the second gas species, CO or CO_2, was

allowed to fill the line. At this point, the desired amount of the water was already contained in the mixing bulb, and contained in the main gas line was the targeted amount of the second species. The valves to the mixing bulb were opened for about 1 hour to allow the two gases to initially mix. Then, while the valves to the mixing bulb were open, the valves to the large evacuated storage bulb were also opened, allowing the gas to mix further, making the mixture ready for use or storage. The procedure generally results in gas mixture ratios within 10% of the targeted mixtures, based on QMS measurements in the main chamber.

3.2 Ice film preparation

For each experiment the ices were grown onto the CsI window, maintained at 12 K, through direct vapor deposition. Before each dosing step, the evacuated gas line was flushed in triplicate with the species to be deposited to prevent contamination of the ice layers, then filled with about 10 Torr of the desired species. With the exception of a few experiments focusing on the effects of the angle of the deposition, the CsI substrate was rotated normal to the deposition tube (0°) during dosing, and the opening of the tube was positioned 8 mm away from the substrate surface. The flow rate of the gas(es) was set to 5×10^{-8} Torr at room temperature, which corresponds to about 5×10^{13} molecules $\mathrm{cm}^{-2}s^{-1}$, or 0.05 monolayer (ML) s^{-1}. After the window was cooled to 12 K, the pure gas, sequence of pure gases (for ice layer experiments) or gas-mixture was introduced into the chamber by opening the precision leak valve to the set flow position. The gas flow rate from the room temperature calibration, along with the IR data collected during deposition were used to approximate the ice thicknesses.

The thicknesses in monolayers (ML) of the different ice components were calcu-

Table 3.1: Spectral parameters

Species	IR feature	Band Pos. (cm^{-1})	Int. Bounds (cm^{-1})	A_{band} (cm $molec^{-1}$)	Density (g cm^{-3})
CO	C–O Stretch	2139	2120-2170	1.1×10^{-17}[a]	0.81[b]
H_2O	O–H Stretch	3280	3000-3600	2.0×10^{-16}[a]	0.94[c]
H_2O:CO_2 Mix	O–H Stretch	3280	3000-3600	1.6×10^{-16}[d]	0.94[e]
CO_2	C–O Stretch	2343	2310-2370	7.6×10^{-17}[a]	1.3[f]
D_2O	O–D Stretch	2453	2225-2700	1.4×10^{-16}[g]	0.94[e]

[a](Gerakines et al. 1995)
[b](Loeffler et al. 2005)
[c](Jenniskens & Blake 1994)
[d](Öberg et al. 2007)
[e]used the same as for H_2O
[f](Escribano et al. 2013)
[g](Venyaminov & Prendergast 1997)

lated using the experimentally integrated infrared spectral features of the deposited ice and band strengths (A_{band}) and ice densities (ρ), using the following equation:

$$N = \frac{\int \ln I_{band} d\nu}{A_{band}}. \tag{3.1}$$

where N is the column density in molecules cm^{-2}, which can be broken down into film thickness (ML or cm) and ρ. The band areas, $\int \ln I_{band} d\nu$, are the absorbance intensities over the specified frequency range for the stretching features of the different species. Table 3.1 lists the band position, integration bounds, band strengths, and solid state densities used for the thickness calculations for each ice species. Because the CsI window is angled at 45° to the IR beam during deposition, the thickness was measured after deposition with the window positioned normal to the beam for verification, and that value was used for experimental calculations. Background spectra

were always acquired on the clean CsI substrate at the beginning of each experiment and subtracted from the recorded sample spectrum afterwards.

3.3 Diffusion experiments

Following the initial ice characterization the sample was quickly heated (5 K/min) to the targeted experiment temperature and was then maintained at this temperature (12–23 K) for 1.5–4.5 hours while monitoring changes in the ice morphology using the infrared spectral features of CO and H_2O, and their dependence on the ice purity/mixing. The first IR spectrum was collected immediately upon reaching the target temperature ($t = 0$) and subsequent IR spectra were collected every two minutes. All IR spectra were acquired with the sample normal to IR beam with a 2.5 mm aperture, 1 cm^{-1} resolution, and 64 averaged interferogram scans per spectrum. During the entire experiment the gas-phase composition was also monitored using the QMS, checking especially for ice desorption.

Chapter 4

Results

Table 4.1 lists the main set of experiments carried out in this thesis. These all consist of an initially layered ice with CO underneath and then either H_2O, H_2O followed by D_2O or CO_2:H_2O mixture layered on top. The mixing of these ice layers as a function of time at specific temperatures was used to characterize and quantify CO diffusion in H_2O ice (mixtures). The following sections begin with a description the IR spectral analysis used to infer the abundances of pure CO and CO mixed with the top ice layers for each experiment and time element, including supporting ice spectroscopic experiments, (§4.1). §4.2 provides a presentation of the effects of ice temperature, thickness, relative CO and H_2O abundance, H_2O porosity and H_2O ice purity on CO mixing using the CO IR band. §4.3 presents the corresponding spectroscopic changes in H_2O and D_2O ice features during CO:H_2O mixing, which provide additional constraints on the CO diffusion mechanism. In §4.4, a simple kinetic analysis is used to extract the diffusion barrier of CO in these experiments, followed by a more detailed diffusion modeling using Fick's diffusion law in §4.5.

Table 4.1: H_2O/CO ice mixing experiments ordered based on the main parameter varied within each subset of experiments, together with exponential fit results (§4.2) and the diffusion rate from Fick's diffusion law analysis in §4.5.

Exp.	H_2O/CO [ML]	α_{dep} [a] [°]	T_{mix} [K]	A_i [b] [% / ML]	k_{diff} [b] [min^{-1}]	A_f [b] [% / ML]	D [c] [cm^2 sec^{-1}]
Ice temperature							
1	34/10	0	12	0.26(0.38)/3	<0.02	N/A	3.8×10^{-18}
2	31/8	0	15	0.49(0.03)/4	0.02(0.01)	0.64(0.02)/5	5.2×10^{-17}
3	35/9	0	16	0.52(0.03)/5	0.07(0.02)	0.65(0.01)/6	3×10^{-16}
4	28/8	0	17	0.44(0.05)/3	0.15(0.05)	0.67(0.01)/5	3.1×10^{-16}
5	31/9	0	20	0.40(0.06)/4	0.78(0.51)	0.64(0.02)/6	2.1×10^{-15}
6	29/10	0	23	0.37(0.07)/4	0.73(0.55)	0.61(0.02)/6	2×10^{-15}
Ice thickness							
7	13/8	0	15	0.46(0.06)/4	0.27(0.35)	0.55(0.03)/4	2.1×10^{-16}
8	59/10	0	15	0.35(0.07)/4	0.06(0.04)	0.56(0.03)/6	1.4×10^{-16}
9	14/9	0	20	0.53(0.03)/5	1.31(3.74)	0.58(0.01)/5	6.7×10^{-15}
10	59/9	0	20	0.44(0.12)/4	0.39(0.22)	0.88(0.04)/8	2×10^{-15}
11	37/5	0	17	0.67(0.28)/3	0.15(0.37)	0.87(0.20)/4	2.6×10^{-16}
12	40/14	0	17	0.10(0.02)/1	0.23(0.04)	0.39(0.01)/5	6.1×10^{-16}
$D_2O/H_2O/CO$							
13	89/81/14	0	15	0.15(0.01)/2	0.05(0.01)	0.42(0.01)/6	8.6×10^{-17}
14	117/106/30	0	15	0.07(0.03)/2	0.02(0.004)	0.33(0.02)/10	5.6×10^{-17}
15	107/86/59	0	15	0.01(0.01)/1	0.03(0.003)	0.17(0.01)/10	5×10^{-19}
Porosity[a]							
16	30/9	30	15	0.49(0.06)/4	0.38(0.22)	0.69(0.02)/6	8.5×10^{-16}
17	14/9	45	15	0.48(0.04)/4	0.61(0.37)	0.65(0.01)/6	6.4×10^{-16}
18	19/8	30	20	0.45(0.04)/4	1.85(2.59)	0.69(0.01)/5	3.3×10^{-15}
19	26/8	45	20	0.56(0.04)/4	1.56(1.56)	0.81(0.01)/6	4×10^{-15}
Reproducibility							
20	34/10	0	17	0.26(0.03)/3	0.09(0.02)	0.55(0.01)/5	2.2×10^{-16}
21	39/10	0	17	0.30(0.04)/3	0.11(0.02)	0.59(0.01)/6	2.9×10^{-16}
22	35/10	0	17	0.32(0.04)/3	0.09(0.03)	0.54(0.01)/5	2.2×10^{-16}
H_2O:CO_2/CO							
23[d]	46/10	0	15	0.27(0.02)/3	0.10(0.04)	0.41(0.01)/4	1.1×10^{-16}
24[d]	34/9	0	17	0.28(0.06)/2	0.11(0.07)	0.49(0.04)/4	9.4×10^{-17}
25[d]	35/10	0	20	0.24(0.04)/2	0.23(0.04)	0.67(0.01)/7	6×10^{-16}

[a] Porosity of the water layer was varied by changing the angle of incidence, α_{dep}, during deposition of the the H_2O.

[b] All experiments were fit to a function of the form $A_i + A_f(1 - e^{-k_{diff}t})$, where A_i is the initial fraction/amount of mixed CO, A_f the final fraction/amount of mixed CO and k_{diff} the mixing fraction rate coefficient.

[c] Calculated by L. Karssemeijer from Radboud University (Lauck et al. in prep)

[d] The top layer was a mixture of 4:1 H_2O:CO_2.

4.1 IR spectroscopy of ice mixing

The basis of this study is the well known spectral profile difference of pure CO ice and CO mixed with H_2O (e.g. Sandford & Allamandola 1988, Fig. 4.1a,b). Pure CO exhibits a Lorentzian IR band profile centered at 2139 cm^{-1} (Bouwman et al. 2007), while the spectral feature of CO in a CO:H_2O ice mixture can be fit by two overlapping Gaussians with peaks centered at 2137 cm^{-1} and 2152 cm^{-1}. Sandford & Allamandola (1988) identified the 2152 cm^{-1} band with CO molecules bound in a repulsive, interstitial binding site among water molecules and is therefore often referred to as the 'polar' band, while the 2137 cm^{-1} band is attributed to CO in an apolar environment, where it is not interacting with the hydrogen bonding network within the water.

Figure 4.1c shows the evolving spectra of an initially layered H_2O/CO ice kept at 17 K for 90 min (Exp. 4). The initial spectra appears to be a combination of a pure CO ice spectra and a CO ice mixture spectra, with the pure CO ice being the main component. Over time, the polar feature increases, and the spectra become similar to the profiles of a completely mixed ice. One of the later spectra (Fig. 4.1d) is well fitted by two Gaussians, and a small Lorentzian, supporting this qualitative assessment that the pure ice is changing to a mixed ice. This kind of fit was automated using the IDL MPFIT function, which was applied to all experiments and time points. Extracting an ice mixture fraction from these fits is complicated, however, by the overlap of one of the ice mixture peaks with the pure CO ice band, making the relative contributions of pure and mixed CO to this part of the spectral band highly uncertain. Therefore, the 2152 cm^{-1} band alone was used to determine the degree of mixing, since it is better resolved from the other features. This approach is possible because of the stable ratio between the total ice mixture band and the 2152 cm^{-1} band area in

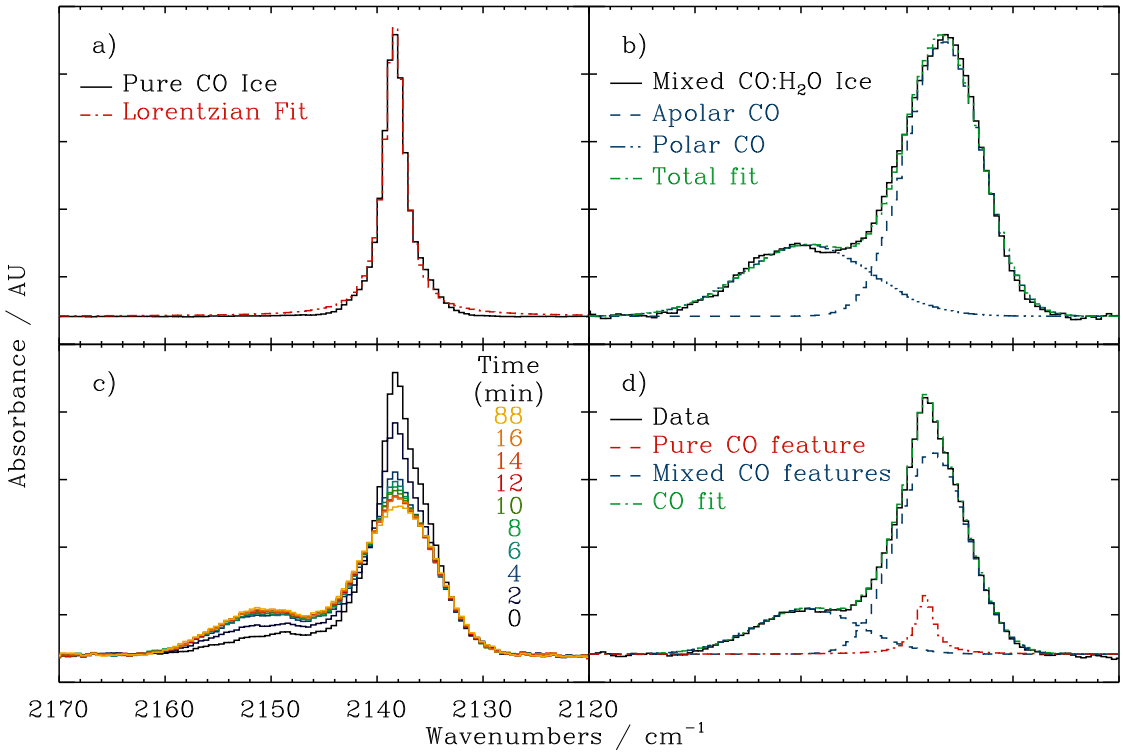

Fig. 4.1.— Spectral changes in pure and mixed CO ice: (a) Infrared spectra of pure CO ice together with a fitted Lorentzian profile, (b) a H_2O:CO 5:1 ice mixture together with the spectral Gaussian fits, (c) the changing spectral features as a H_2O/CO layered ice mixes, and (d) the fit of pure and mixed CO ice components to an experiment spectrum from (c) using the Lorentzian and Gaussian functions from (a) and (b). Each panel spans the same frequency range. In panel a the absorbance scale reaches 0.012 AU (IR absorbance units), while panels b, c, and d are on the same scale reaching 0.003 AU.

$CO:H_2O$ ice mixtures (Fig. 4.2), including 1:10 and 1:2 $CO:H_2O$ ice mixtures, and a mixture that also contains CO_2. The consistency of the polar feature ratio at about 3 indicates that it is insensitive to the mixing ratio of $CO:H_2O$ and also to other minor mixture constituents.

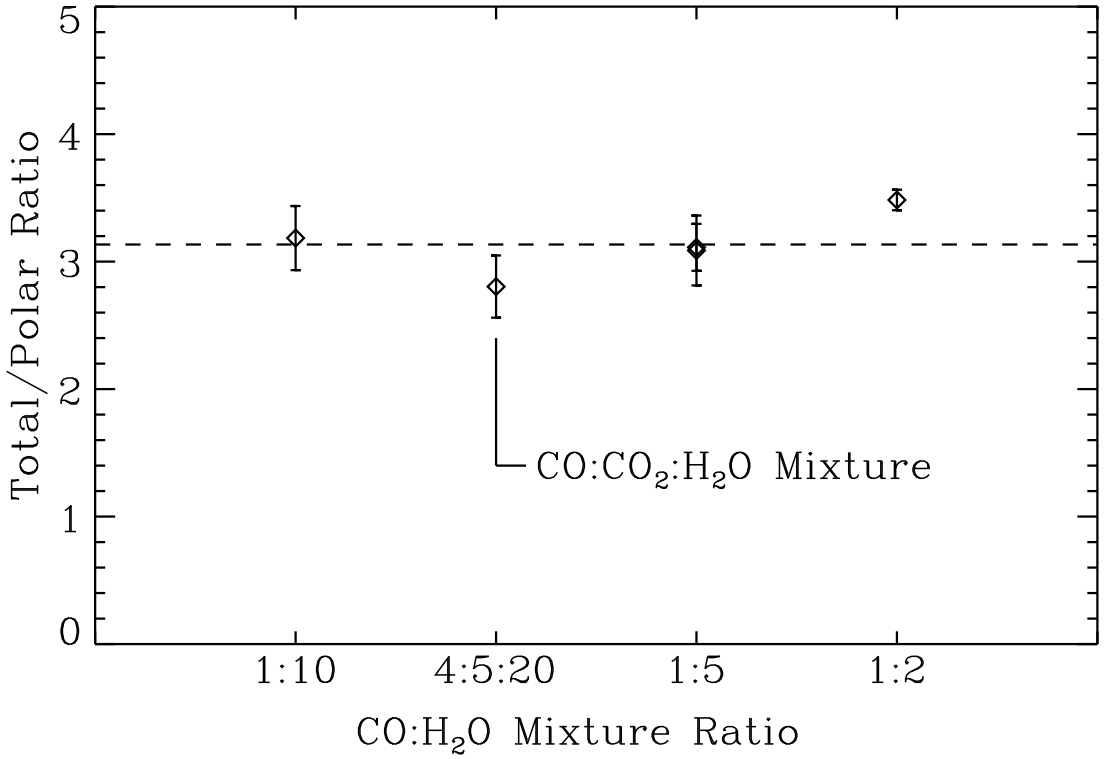

Fig. 4.2.— The ratios of the total CO over the 'polar' 2152 cm^{-1} spectral feature of CO in mixed ices are consistently ∼3 over a range of mixture ratios and compositions.

Based on these results, mixing of the layered ices was analyzed using the contribution of the 2152 cm^{-1} spectral feature to the total integrated band area. To determine this ratio, the CO band was always fitted with one Lorentzian and two Gaussian functions. The calculated areas from each of the fit functions were used to quantify the amount of mixed CO, assuming a factor of 3 between the 2152 cm^{-1} feature and total area of the mixed CO contribution, i.e. the fraction of CO mixed

in with the H_2O was calculated from $\int I_{2152\,\mathrm{cm}^{-1}} d\nu \times 3 / \int I_{\mathrm{CO}} d\nu$.

4.2 CO diffusion experiments

H_2O/CO ice mixing was studied by varying a large range of experimental parameters (Table 4.1). Together these experiments explored the effects of mixing temperature (12–23 K), CO and H_2O ice thickness (5–60 ML and 13–114 ML, respectively), H_2O/CO abundance ratio (1.5–12), H_2O ice porosity (using different deposition angles), and H_2O ice composition (investigated by adding CO_2) Additional experiments were added to test experimental reproducibility and the utility of isotopic labeling of H_2O ice layers to constrain the diffusion rate of CO through the ice.

Figure 4.3 shows the time progression of CO mixing with the H_2O ice for most of the experiments listed in Table 4.1; a couple of the *mixing temperature* experiments are excluded for visual clarity and the isotopically labeled experiments and the ones including CO_2 ice are treated separately in a later section. Above 12 K, all layered ice experiments show signs of mixing within the first few minutes, and the final mixing fraction is typically reached within tens of minutes. We fit the experiments with an exponential function $A_i + A_f(1 - e^{-k_{\mathrm{diff}}t})$, where A_i is the initial fraction of mixed CO, A_f the final fraction of mixed CO and k_{diff} the mixing rate, which generally fits the experiments well. For some experiments, specifically 5, 6, 7, 9, 10, 11, 12, 16, 17, 18, and 19, this kind of exponential analysis could only be applied to the first 5–20 data points in order to obtain a good fit to the data, and the significance of this is discussed later. The resulting fit coefficients and their uncertainties are listed in Table 4.1. Across the experiments the initial fraction of mixed CO ice corresponds to 3–5 ML (with a few exceptions noted below), which thus seems to define the interface thickness of CO and amorphous H_2O ice, which inherently mixes

upon water deposition.

In panel a of Figure 4.3, it is clearly observed that the ice mixing rate increases as a function of ice temperature between 12 and 20 K when all other parameters are kept constant (Exps. 1–6), and the growth curves are well fitted with our exponential function. This result together with the observation that the final mixing fraction does not depend on the mixing temperature, suggests that the mixing of the ices in this temperature range can be described by a single diffusion process. Between 15 and 23 K, the mixing rate increases from 0.02 to 0.8 min^{-1}, where the mixing rate is measured as the fraction of the CO ice mixing with H_2O. The final amount of mixed CO consistently approaches a fraction between 0.6 and 0.7. Also at the higher temperatures (20 and 23 K), the final spectra were comparable to a mixed ice profile within the experiment timeframe, while the lower temperatures still had some clear indications of the pure CO ice feature.

To investigate the effect of layer thickness on the ability for CO to mix into the water layer, a few sets of experiments were performed with varied layers for both CO and water. When the thickness of the water layer was varied, there were no clear trends in the mixing rate at either 15 K or 20 K. However, final mixed fraction of CO increased with increasing H_2O coverage. It is also worth noting that for the thicker water ice, the exponential fit deviated from the data beyond 1.5 hours, potentially indicative of a second diffusion process.

As expected, both the initial and final mixed fractions of CO decrease with increasing thickness of the CO layer (Fig. 4.3d) between 5 and 14 ML at 17 K. The initial fraction of mixed CO decreased from 0.7 to 0.1 as the layer thickness was increased. The final mixed fraction decreased as well, from 0.9 for 5 ML of CO to 0.4 for 14 ML of CO. Also, there was a slight increase in the mixing rate, from 0.15

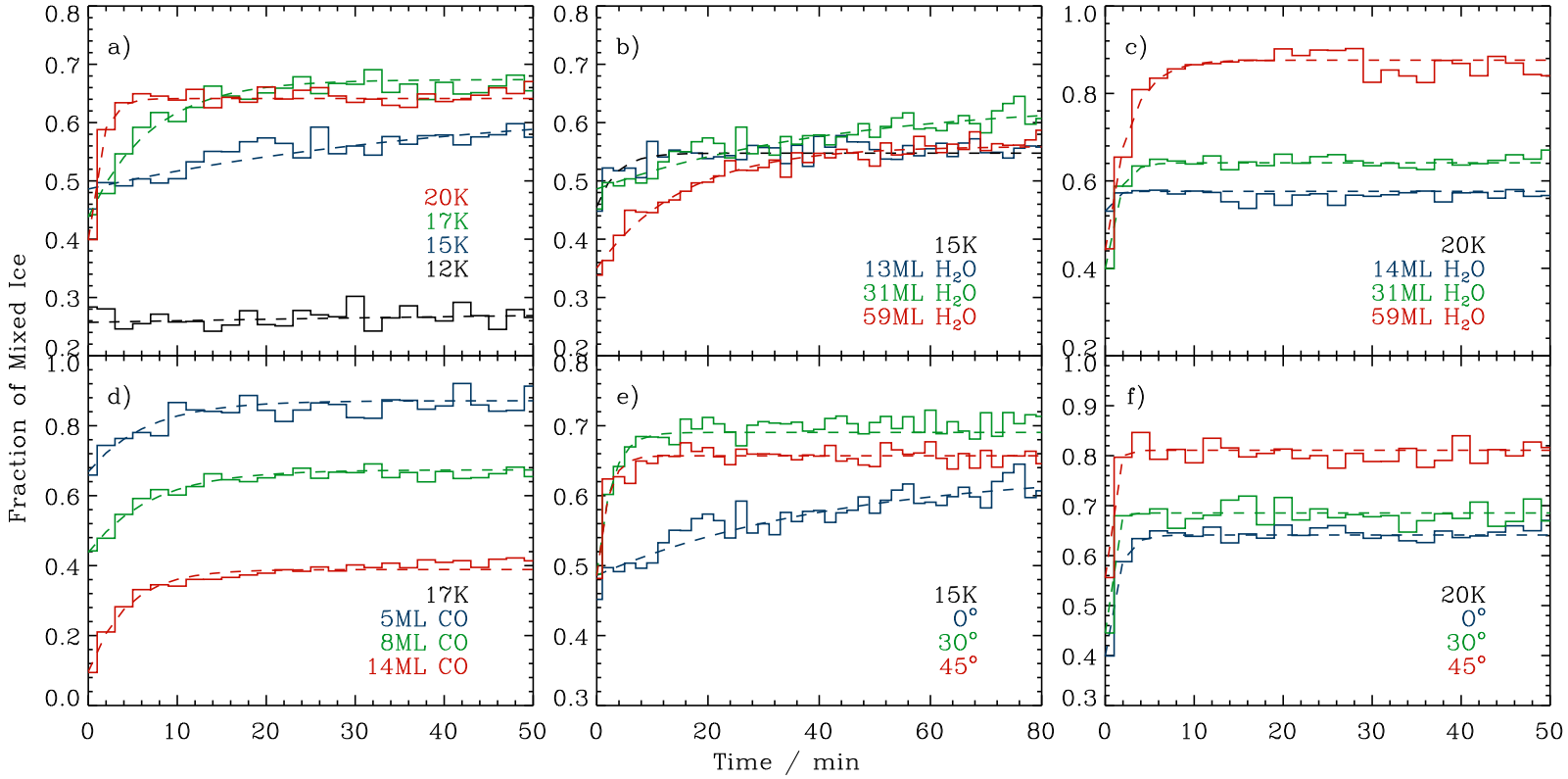

Fig. 4.3.— The fraction of mixed CO ice as a function of time in initially layered CO/H_2O ices. Panel a) shows that the mixing rate increases when comparing experiments with temperatures ranging from 15K to 20K, and they all reach a similar final mixed amount; at 12K there was no significant mixing detected. Panel b) and c) shows the mixing in experiments with varying thicknesses of the water layer at 15 and 20K, but a constant CO ice thickness of 10 ML. Panel d) shows the mixing of CO in experiments with varying CO thicknesses at 17K and the H_2O ice layer kept constant. Finally the curves in panel e) and f) show CO mixing in experiments with varied water layer porosity (increasing with higher angles of deposition) at 15K and 20K.

to 0.23 min^{-1}, with increasing CO layer thickness, perhaps indicating that when the ratio of CO to water becomes greater, the water matrix may have different properties, enabling a different mixing process.

In the separate set of experiments incorporating a third D_2O layer, the thickness of the CO layer was also varied, but the layers were significantly thicker and the experiments were performed at 15 K. The CO layer was varied from 14 to 59 ML, while the total water layer (H_2O and D_2O) ranged from 143 to 161 ML. Similarly to Exp. 12, the initial amount of mixed CO from the thicker layers ranges from 1 to 2 ML. In contrast to the thinner layer experiments, but also as expected, the CO band spectral fits were dominated by the pure Lorentzian feature, with small mixed features increasing over time. However, the mixing rate was comparable to the rate from Exp. 2 also at 15 K, indicating that the rate not affected in thicker ices. The final mixed amount of CO in both Exps. 14 and 15 is 10 ML, so even though the thickness was doubled, the amount of CO able to mix over a 4 hour period was the same, further supporting the claim that the rate is independent of ice thickness in thicker ice films.

Finally, Figure 4.3e,f show the effect of H_2O ice deposition angle on the CO diffusion. Based on previous experiments (e.g. Kimmel et al. 2001; Raut et al. 2007), an increasing deposition angle results in a more porous H_2O ice when the ice is deposited at low temperatures. The CO mixing rate clearly increases with ice porosity in our experiments; from 0.02 to 0.52 min^{-1} at 15K and from 0.78 to 1.88 min^{-1} at 20K. By contrast there are no obvious trends with regard to the initial or final mixing fraction. It should also be noted that the CO band had a somewhat different shape compared to the compact ice experiments, but our spectral fitting procedure still worked well.

In separate set of experiments (Exps. 23–25) the effect on CO diffusion following

the addition of CO_2 to the water ice was examined. This is an important aspect for interstellar applications, where CO_2 is found to be mixed in with the observed H_2O ice (Pontoppidan et al. 2008). In these experiments, ∼40ML of a 1:4 CO_2:H_2O mixture was layered on top of ∼10 ML of CO, and the temperature was varied from 15 to 20 K. The initial fraction of mixed CO ice was consistent at 0.3 for the three experiments, corresponding to 3 ML of CO, again representing the interface between the layers. Both the mixing rate and the final mixed fraction increased with temperature, from 0.10 to 0.22 min^{-1} and 0.49 to 0.69, respectively (Fig. 4.4). In the 15 and 17 K

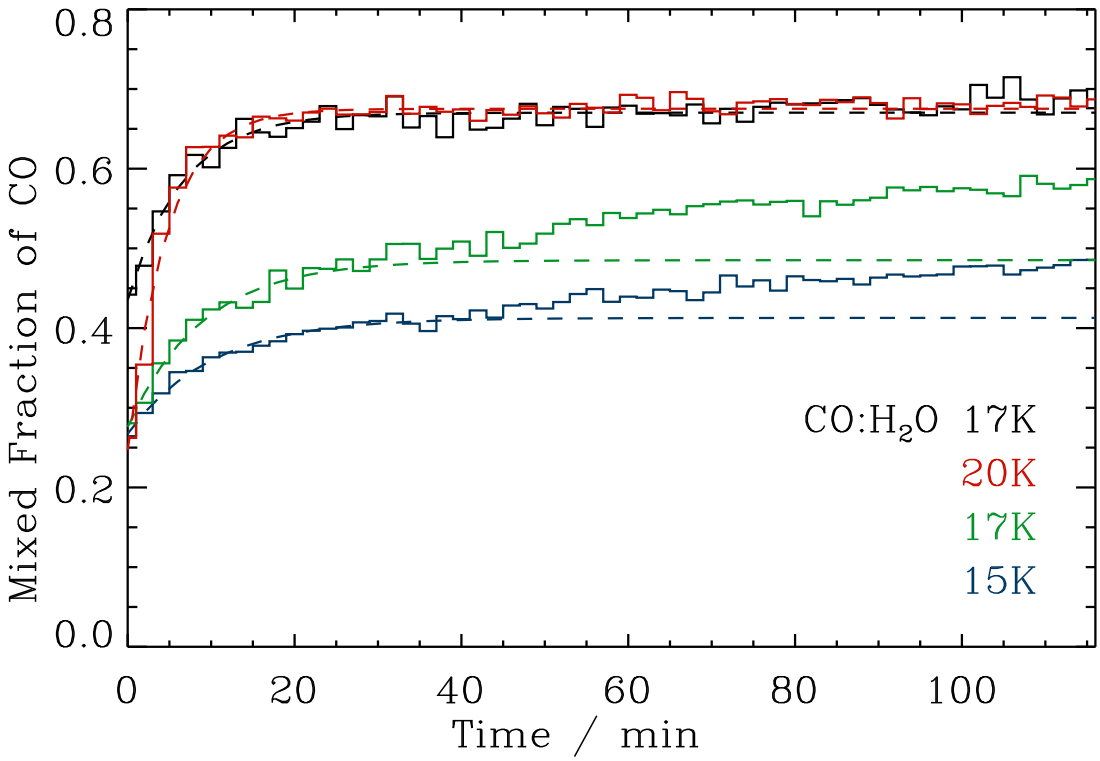

Fig. 4.4.— The mixed CO fraction versus time in the CO_2:water mixture experiments. The result from the 17K pure water experiment is given as a comparison.

experiments, the exponential fit deviated from the data beginning at 30–40 minutes when the mixed fraction continued to gradually increase. After the point where the exponential fit deviates, the data appear to trend toward the mixed fraction level

that was reached in the 20 K experiment if the experiments were extended for more time. Compared to the H_2O/CO mixing experiments with ice layer thicknesses and temperatures, the CO_2 mixture experiments display less of a temperature dependence with regard to the diffusion rate, and in general, the CO takes longer to mix into the CO_2:water mixture.

4.3 H_2O ice spectroscopy

The H_2O (and its isotopologue) infrared bands are also affected by mixing (Rowland et al. 1991; Bouwman et al. 2007), and measuring these changes can provide both a check on the CO results and potentially additional information with isotopically layered water ices. On the blue end of the OH stretching band in the water IR spectrum, there are small signatures from OH bonds that are not interacting with the hydrogen bonding network within the bulk of the water ice. These specific OH bonds, called dangling OH bonds, are found at the outer surface of the ice film, or on the walls of pores within the ice. The profile of the dangling OH bond feature changes as pure H_2O becomes mixed with other molecules, like CO or CO_2. The dangling bond band in pure water is a double feature, with positions at 3700 and 3720 cm^{-1}, and the band at 3700 cm^{-1} being slightly larger. As other molecules mix with the water, the dangling OH feature changes into a broader, single band that is redshifted to 3655 cm^{-1} (Fig. 4.5a). The corresponding dangling OD bands (pure at 2750 and 2730 cm^{-1}, mixed at 2690 cm^{-1}), behave in the same way as the D_2O ice mixes.

Using these spectral changes in the water features, the mixing can be monitored from a different perspective. Although the features are subtle due to the relatively thin layers of H_2O and D_2O deposited (as opposed to 1000s of monoloyers where the features are more intense), when comparing subtracted spectra, the changes are clear;

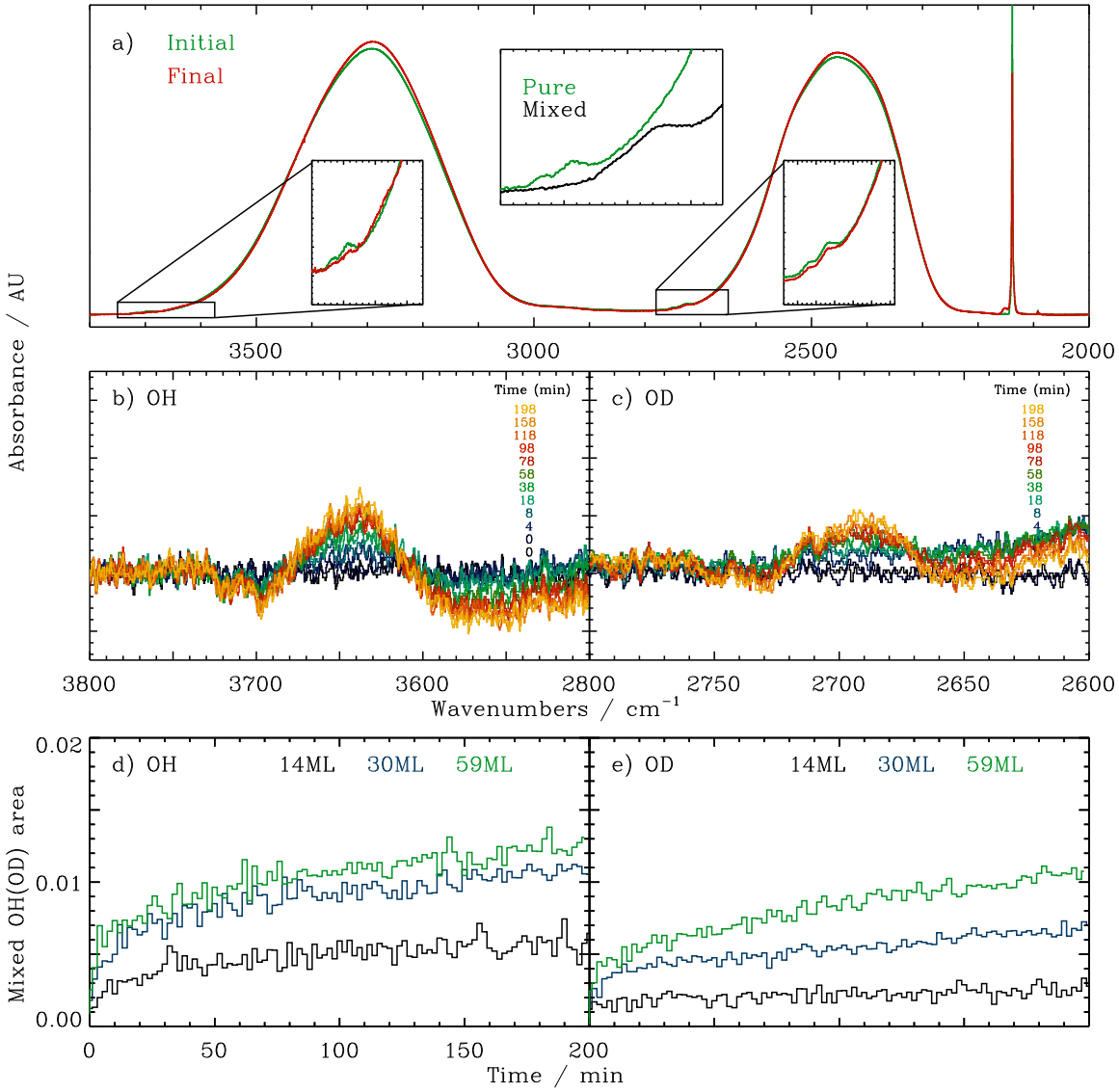

Fig. 4.5.— Spectra in a) are overlaid initial and final spectra from experiment 14, while insets 2 and 3 show the spectral differences in the dangling OH and OD feature during the experiment. Inset 1 shows a pure water ice compared to a premixed water:CO mixture. The time evolution of the spectral change (from subtracted spectra) shown in panel b) for OH and c) for OD clearly shows the decrease in the the double feature at 3700 cm^{-1} and increase in the broad single feature at 3650 cm^{-1} during mixing. The increasing area of the mixed dangling OH and OD features are plotted versus time in d) and e), respectively.

the broad feature at 3655 cm^{-1} increases while the small pure features decrease for both the OH and OD bands (Fig. 4.5b,c). The OH features appear to change sooner than the OD features, and the final intensity of the changes is greater for the OH bands.

The integrated areas of the increasing mixed OH band from 3680–3610 cm^{-1} and OD band from 2715–2670 cm^{-1}(Fig. 4.5d,e) qualitatively show that the CO is mixing into the water layer more quickly than into the D_2O layer.

4.4 Kinetic analysis

As Fig. 4.3 shows, most of the mixing time series can be fit by a single exponential fit (the most notable exception is the H_2O:CO_2 mixture experiments). This suggests that the mixing of thin CO and H_2O ices can be characterized by a single diffusion process and therefore a single diffusion barrier. To test this, Fig. 4.6a shows the fit of the mixing rates derived from experiments 1–6 (where all parameters except for temperature were kept constant) to the Arrhenius equation,

$$k = \Gamma \times e^{-E_{\mathrm{diff}}/T}, \tag{4.1}$$

where Γ is the pre-exponential factor, E_{diff} the diffusion barrier in K, and T the ice temperature. When a linear fit is applied to $\ln(k)$ versus $1/T$, the E_{diff} is determined by obtaining the slope of the line. The resulting barrier is 163±31 K, or 14 meV.

We also applied the Arrhenius equation to all other subsets of experiments where all experimental parameters except temperature were kept constant, including H_2O/CO experiments with ice thicknesses of ∼14/8 (thin) and 59/10 (thick), and different porosities defined by the deposition angle, and the H_2O:CO_2 ice mixture layered on

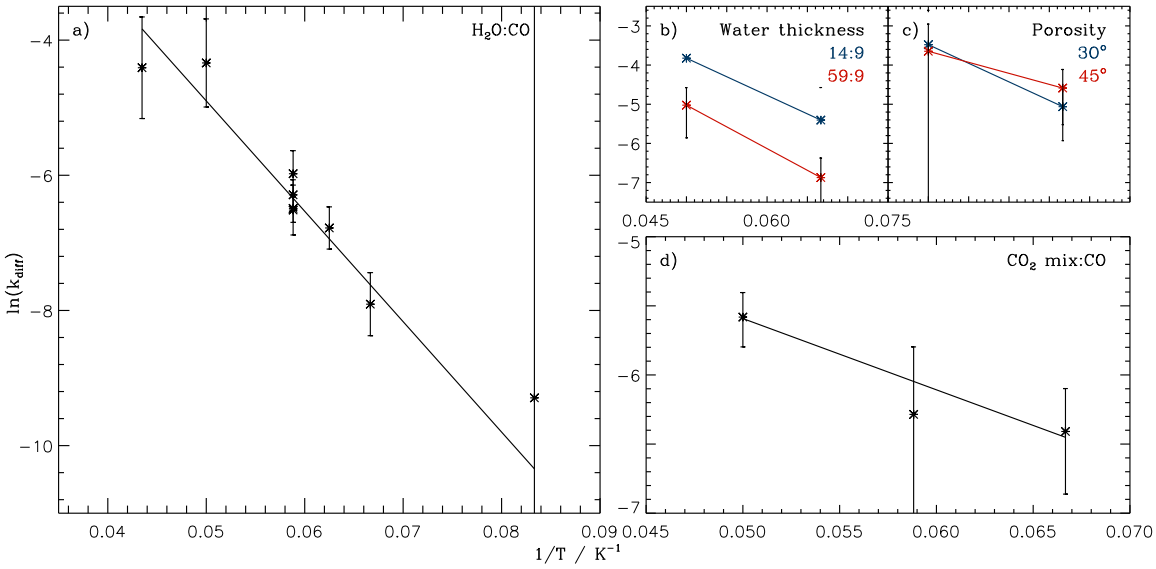

Fig. 4.6.— Arrhenius plots incorporating the rates from Exps. 1–6, and 20–22 are plotted in panel (a), the mixing rates from the water thickness and porosity experiments plots in (b) and (c), and the H_2O:CO_2 ice mixtures in panel (d).

top. In most of these cases the resulting barriers and pre-exponential factors are very uncertain since the fit is done with only 2 or 3 points. Figure 4.6 shows the resulting plots, and Table 4.2 lists the extracted values for Γ and $E_{\rm diff}$. Within the uncertainties, all compact H_2O/CO mixing experiments result in the same diffusion barrier. By contrast, the most porous ices, deposited at 45°, and the H_2O:CO_2 ice mixtures result in a significantly lower CO diffusion barrier of ∼50–100 K.

Table 4.2: Calculated energy barriers and pre exponential factors assuming an Arrhenius-type mixing process.

Experiment	Exponential			Fick's		
	Γ [sec^{-1}]	E_{diff} [K]	E_{diff} [meV]	Γ [cm^2 sec^{-1}]	E_{diff} [K]	E_{diff} [meV]
Mixing temperature	26(2)	163(31)	14	5.4×10^{-12}	168	15
Thin water layer	3(12)	95(188)	8	2.2×10^{-10}	208	18
Thick water layer	2(3)	111(52)	9	5.8×10^{-12}	160	14
Porosity, 30°	4(6)	95(91)	8	1.9×10^{-13}	81	7
Porosity, 45°	0.4(4)	56(70)	6	9.8×10^{-13}	110	9
CO_2 mixture	0.05(1)	52(24)	4	8.1×10^{-14}	104	9

4.5 Diffusion modeling

The dependence on temperature was explored by applying the Arrhenius equation, but the mixing behavior may also be affected by the morphology and thickness of the layers. The simple exponential analysis does not have the capability to account for the thickness differences in the experiments. In order to get a better understanding of the diffusion parameters, independent of the thickness variances, an analytical model that incorporates the ice thicknesses was needed. With a successful model, the components of the exponential and preexponetial terms can be broken down to extract the barrier and diffusion coefficient more accurately. Fick's 2nd Law of Diffusion has been used recently (Karssemeijer et al. 2014; Mispelaer et al. 2013) to describe CO diffusion in water at temperatures 35 K and above. In a collaborative effort with the Cuppen group at Radboud Univeristy, this method was applied to the experiments presented here.

In general, Fick's 2nd Law describes the behavior of a species within a diffusive system with respect to time and position. The law states that

$$\frac{\partial n(z,t)}{\partial t} = D(T)\frac{\partial^2 n(z,t)}{\partial z^2}. \tag{4.2}$$

With respect to these experiments, n is the amount of CO in the ice film, t is time, z is the thickness of the ice with 0 being at the substrate surface, h at the vacuum surface, and d at the CO:H_2O interface, and $D(T)$ is the diffusion coefficient (dependent on temperature, T).

For this layered ice approach, at temperatures below the CO desorption temperature, the total amount of CO in the system is constant, but the amount of mixed CO increases over time. Therefore the initial conditions for the amount of CO in the

system, n_0, remain constant during the experiment; they are expressed as

$$\int_0^\infty n(z,t)dt = \int_0^h n(z,t)dz = n_0. \tag{4.3}$$

Because CO can never escape from either the substrate ($z = 0$) or the vacuum ($z = h$) surface of the ice film, there is an absence of CO flux at both of those surfaces, and therefore the boundary conditions are

$$\frac{\partial n(0,t)}{\partial z} = \frac{\partial n(h,t)}{\partial z} = 0. \tag{4.4}$$

Applying these initial and boundary conditions yields the following solution to Fick's 2nd Law:

$$n(z,t) = \frac{n_0 d}{h} + \sum_{i=1}^{\infty} \frac{2n_0}{i\pi} \sin\left(\frac{i\pi d}{h}\right) \cos\left(\frac{i\pi z}{h}\right) \exp\left(-\frac{i^2\pi^2}{h^2} Dt\right) \tag{4.5}$$

where n_0 is the amount of total CO, and i is the iteration in the series. The amount of mixed CO is represented by integrating this solution over z from d to h. The final expression is

$$n_{\text{mixed}}(t) = \frac{n_0 d}{h}(h-d) - \sum_{i=1}^{\infty} \frac{2n_0 h}{i^2\pi^2} \sin^2\left(\frac{i\pi d}{h}\right) \exp\left(-\frac{i^2\pi^2}{h^2} Dt\right). \tag{4.6}$$

Qualitatively, the model shows the amount of mixed CO versus time increases exponentially and then levels out to its final mixed state. For the amount of CO as a function of position within the ice film, at $t = 0$, almost all of the CO is located from 0 to d, and almost none from d to h. As time goes on, the CO diffuses across the interface d, and gradually the amount of CO from d to h increases, while it decreases from 0 to d, until the film is fully mixed at $t = \infty$, e.g. Fig. 4.7.

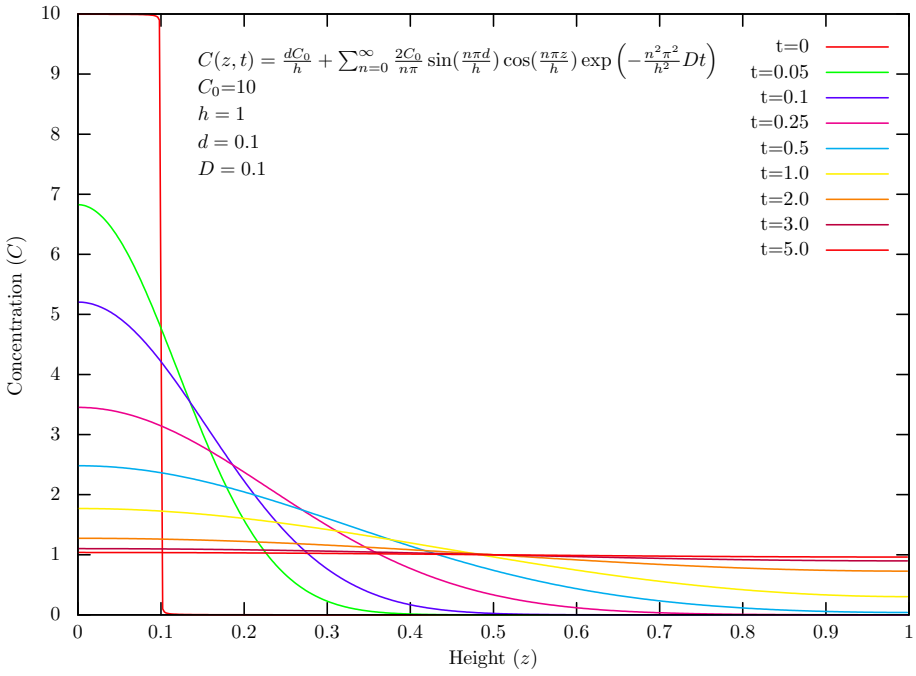

Fig. 4.7.— The concentration of CO with respect to position, at various time points.

This model provides an excellent fit to all the experimental data except for the very thin-layered experiments. Figure 4.8 shows both analyses' fits overlaid on the data. The model fit was used to solve for the diffusion coefficient, D, at each time point, and the results are listed in Table 4.1. The results for D show analogous trends as the mixing rate parameter extracted from the exponential fits.

The results for the energy barrier calculations derived from the Arrhenius analysis using the D values (listed in Table 4.2) are comparable, within the uncertainties, to the barriers from the k_{diff} results for the data sets for pure compact water. However, the barriers for the high-porosity water, and the CO_2 mixture were greater with the Fickian analysis than the exponential analysis. In both analyses, the CO diffusion resulted in a lower calculated energy barrier for the more porous water layers, and the CO_2 mixture layer, compared to the compact pure water layers.

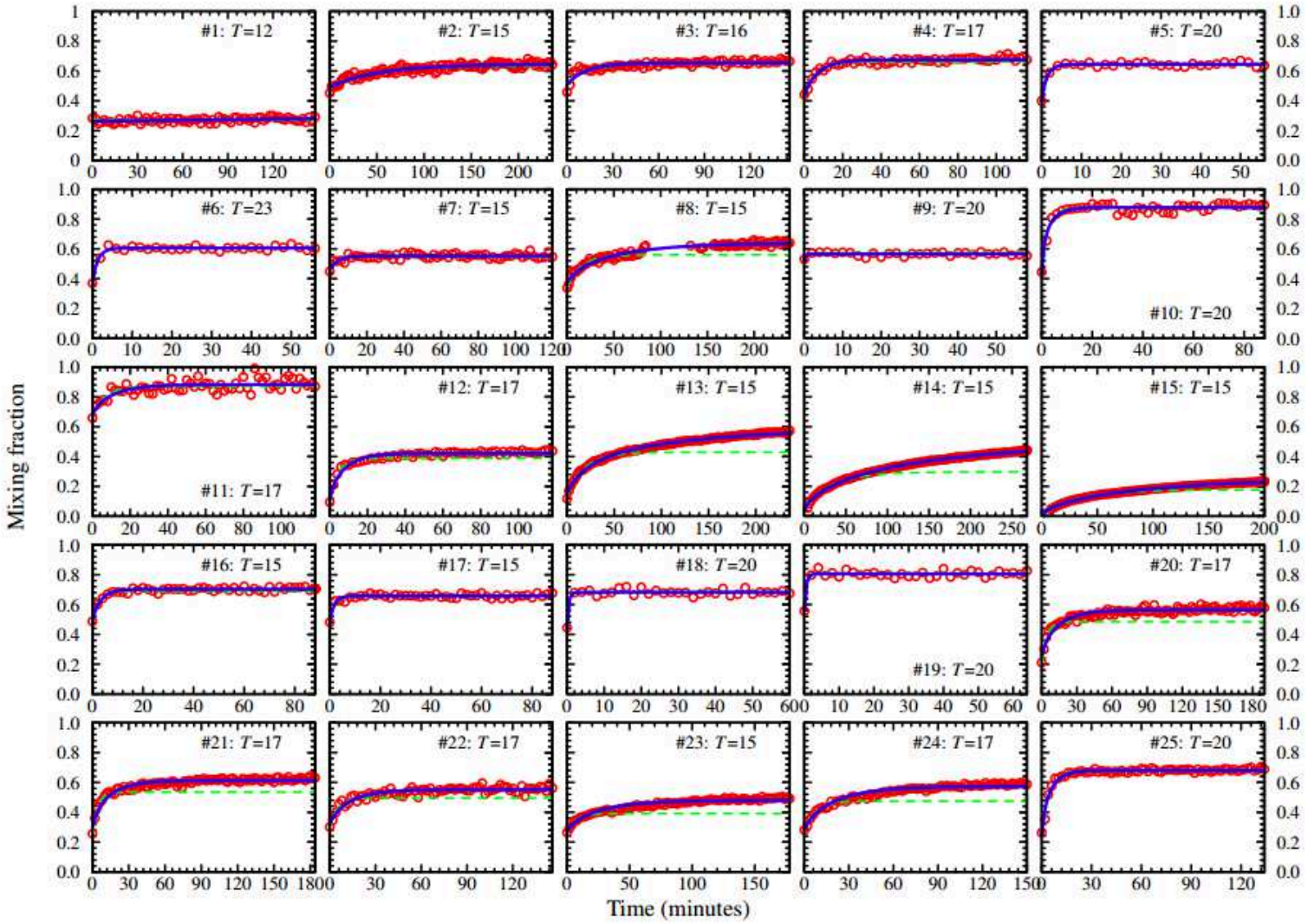

Fig. 4.8.— Solutions of the Fickian model (solid blue lines) and the exponential fits (dashed green lines) for all experiments.

Chapter 5

Discussion and implications

5.1 The CO diffusion barrier

According to the presented results, the barrier for CO to diffuse into H_2O ice is less than 200 K, with a best fit value of 170 K. This value is comparable within the uncertainties of results from previous studies on CO diffusion in amorphous H_2O ice using three different approaches: segregation of CO from CO:H_2O ice mixtures (Öberg et al. 2009), CO desorption from CO:H_2O ice mixtures (Karssemeijer et al. 2014), and CO desorption from layered H_2O/CO ices (Mispelaer et al. 2013). The derived CO diffusion barriers in these studies all range between 120 and 300 K (10–30 meV), though Karssemeijer et al. (2014) conclude that this low barrier only describes the weakest bound CO population in the ice, which is the most likely CO moving by surface diffusion. It is quite remarkable that the results are in such agreement considering the very different experimental conditions used in these studies in terms of vacuum and deposition conditions, ice thicknesses and ice morphology. With this result being reproduced by several different labs and experimental methods, the low CO diffusion barrier (<25% of the CO binding energy on H_2O ice) seems to be a

robust result.

Of the four different methods that have been used to derive the CO diffusion barrier, this approach is arguably the most straightforward to measure diffusion of weakly bound CO in H_2O ice, since it only includes a single process (CO diffusion into H_2O ice), and starts off with pure, rather than pre-mixed ices. Measuring CO diffusion by desorption or in mixed ices involves an ensemble of processes, each with its own barrier perhaps, as the CO makes its way out of the matrix. Based on the presented set of experiments the smallest barrier that CO needs to overcome in order to diffuse in H_2O ice is thus 170±30 K. There are some indications that this barrier is even lower in very porous ices, and when the H_2O ice is mixed with CO_2, which is both astrophysically significant and provides clues on the diffusion mechanism in these experiments.

5.2 The CO diffusion mechanism

Diffusion inside of H_2O ice can theoretically occur through several different mechanisms, including molecular swapping (Öberg et al. 2009), and diffusion in nano- and micropores, where the latter is indistinguishable from surface hopping (Karssemeijer et al. 2014). Additionaly, the mechanism could change as CO or other molecules enter into the ice, since they may add sites with lower binding energies that CO may preferentially hop between. Based on the derived low diffusion energy barrier of 170 K, we can rule out the swapping mechanism, as this bulk diffusion process would require more energy. Furthermore, the loss of the spectroscopic feature identified with free OH stretches and its replacement with a spectral band characteristic of free OH-CO interactions demonstrates that CO occupies available sites along pore walls in the ice. Therefore, as similarly indicated in previous studies, CO diffusion in these

experiments is concluded to be pore-mediated.

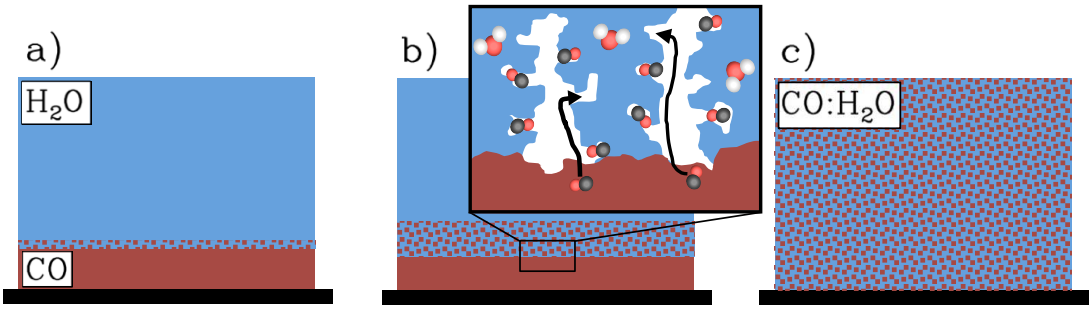

Fig. 5.1.— Schematic of the mixing process. The layered system at $t = 0$ is shown in a). Represented in b), mixing occurs, with the inset showing the CO molecules diffusing along the micropore surfaces into the strong-binding nanopore sites. After some period of time, the layer becomes fully mixed, shown in c).

Figure 5.1 shows a schematic of the proposed mixing mechanism of the CO and H_2O ices through CO diffusion into the H_2O ice via pores. Shown in panel a of the figure, the ice layers at the start of each experiment have a thin interface where mixing has already occurred, but this mixing (only up to a few MLs) is due to the initial interactions of CO and water upon water deposition and during the short warm-up, instead of true diffusion and migration of the CO through pores in the water layer. Karssemeijer et al. (2014) showed that these pores have two different binding sites, which have been identified with the two spectral bands characteristic for CO mixed into H_2O ice. We only follow the growth of the spectral band attributed to the CO population that is strongly bound to H_2O. The growth of this CO population may still be governed by hops between low-energy barrier sites, if several hops are needed before finding a strong-binding site, with a high-energy barrier required to escape, and the probability that a CO molecule can hop out of such a site is negligible. The observation that CO can diffuse through more than 70 ML of H_2O ice (Fig. 6) strongly supports this scenario, i.e. each CO molecule diffuses through the H_2O ice pores until it finds a high-energy binding site, a nanopore, which means that as more

CO is diffusing into the ice each molecule has to diffuse for a longer time until it finds an empty, available nanopore. The expected bottom-up mixing is supported by the layered D_2O/H_2O experiments, which show that the nanopores in the H_2O ice layer are filled faster compared to the D_2O nanopores.

An effort was made by our collaborators to characterize the mixing rate of the second, freely mobile CO population directly by measuring the mixed feature at 2137 cm^{-1}. While the overlap between this feature and the spectral feature due to pure CO prevented any absolute determination of the mixing rate, it was possible to obtain a set of relative rates for a subset of experiments and therefore a diffusion barrier. Within the uncertainties, this barrier was in good agreement with the one derived from the strongly bound CO population, but the errors are too large to use this result to put any additional constraints on the diffusion process.

Based on these results, the CO diffusion into low-porosity H_2O ice should be dominated by a single process, hopping along the H_2O micropore walls, and a single energy barrier, the weak bond between CO and H_2O in binding sites where CO is not interacting with the hydrogen-bonding network in the water. By attempting to parameterize the mixing rate as an Arrhenius type process (see eq. 4.1), it is assumed that the rate (k), or number or successful hops per second, is described by a pre-exponential factor (γ) and the probability for the hop to occur (the exponential term). That probability is dependent on energy required for the hop and on the temperature. The pre-exponential term is not well understood, but one theory is that it may be related to an attempt frequency, i.e. attempts for the CO molecule to try to make the hop into a different site, or perhaps the number of attempts within one monolayer. In the Arrhenius plots, the CO diffusion rate constants had good linear agreement for both the simple exponential analysis and the Fick's diffusion

model analysis, indicating that the process exhibits Arrhenius behavior, with a low energy barrier.

The diffusion behavior and barrier required for the process can be interpreted from the mixing in the early stage of the experiment, just as the CO mixes past the interface into the water layer. Both analyses used only the first several time points (<20 mins) for many of the data sets in order to obtain optimal fits with the respective models, and comparable diffusion barriers were obtained, suggesting that the behavior of the process was reflected in just the first several minutes as CO made it past the layer interface. The Fickian model fit the data better at later times for some of the experiments because it incorporates more information about the experimental conditions, i.e. thickness. The model solution (eq. 4.6) expands the simple exponential to include the thicknesses of the CO and water layers as terms in the pre-exponential and exponential terms, and specifies the interface between them, so that the diffusion process can also be described in terms of position as it diffuses upward into the ice layer. However, because the model only describes CO movement, only scenarios in which the CO is diffusing in a water-dominated matrix are represented well. With thin ice layers (<10 ML), the mixing is due to the initial interactions at the interface upon water deposition, instead of a true diffusion process.

Results suggest that this diffusion is a relatively quick and easy process, but interpreting the low diffusion energy barrier of ∼170 K that was calculated from both analyses is not trivial. The analyses assume that the CO hopping mechanism is a basic first-order kinetic process, dependent on the number of sites available for the CO to diffuse into. In the thicker water layer studies, it is clear that there is a trend in the increasing final fraction of mixed CO, correlating to an increase in available sites.

The nature of these weaker-binding sites is still not well constrained, but it is assumed to be a site along the wall surface of a micropore of the water matrix. If the micropores are large enough, one might consider the possibility of CO diffusing into the micropores, and coating the micropore surfaces as it moves along, instead of continuing to hop along the water molecules on the micropore surface. Then subsequent molecules would follow, or "piggy-back" along one another, and diffuse along the CO coating layer until it reaches the bare, uncoated water site in the micropore pathways. This theory may be likely in highly porous ices, with pore pathways wide enough to accommodate more than a few molecules across. According to Raut et al. (2007), the diameter of pores in a water layer deposited with a collimated flux and normal to the substrate are thin, <3 molecule widths in diameter. Therefore, the main set of experiments in this work would most likely not support this coating theory. Because water deposited at greater angles have higher porosity (Kimmel et al. 2001; Raut et al. 2007), those matrices with mesopores described earlier may very well have large enough pores where this could occur. If this is the case, then the barriers calculated in the main experiments (with low porosity water layers) reveal the energy required for CO–H_2O diffusion, and the slightly lower barriers calculated for the high porosity studies may be indicative of CO–CO diffusion. Because the porosity studies were only fit with two temperature experiments for the Arrhenius analysis, the calculated barriers have a high uncertainty, and we cannot say with confidence that the values are significantly lower than in the compact water at this point to confirm or falsify this theory. More work is needed to explore the porosity effects.

In addition to the porosity, the composition of the water layer may have an effect on the water morphology and the CO diffusion mechanism. In the CO_2 mixture

layer studies, the calculated barrier is 30% lower than in the pure water experiments. This lower barrier indicates that the CO is able to diffuse easier into the mixture compared to the pure water. The binding energy of CO to CO_2 is less than CO to H_2O (Cleeves et al., *in prep*), so it is intuitive for the diffusion barrier to be lower in a matrix that has CO_2 rather than just pure water. Interestingly, the calculated diffusion rate coefficients for CO mixing into the top layer was higher for the pure water studies. One hypothesis is that the CO_2 molecules are occupying the nanopore sites in the premixed layer, and therefore making it more difficult for the CO molecules to find an available nanopore. Because the measurements were based on the signal attributed to CO interacting with the dangling OH bonds in a nanopore, a slower rate in a matrix that has blocked nanopore sites would be expected. If there are less nanopores available, then the time for a CO molecule to find a nanopore site would be longer.

In summary, the CO diffusion observed in this work occurs via pore pathways within the water matrix. The process is the same in all cases: CO diffusing by a hopping mechanism into a weakly-bound site within the pores. In environments with varying morphologies, i.e. porosity and composition, the energies required and nature of the diffusion sites may be different. The experimental evidence presented yields a robust energy barrier result for CO diffusion into a low-porosity amorphous water layer, and give some clues about how the diffusion is affected by varying the water matrix conditions.

5.3 Astrophysical implications

Based on this study CO diffusion in H_2O ice is significantly easier compared to what is assumed in current astrochemical models. Two factors limit the direct application

of these results to astrophysical ices, however. First, even though these experiments were carried out with low-porosity ices, the expected porosity fraction of ∼10% (Raut et al. 2007) is still higher than what is observed in interstellar ices, based on the absence of a free OH-stretch band in interstellar ice spectra, as well as theory (Garrod 2013b). Pore-mediated diffusion may therefore not be important, or even possible, in interstellar settings. Second, interstellar ices are not expected to be pure, and as shown in these experiments, adding CO_2 to the ice may lower the diffusion barrier.

In an astrophysical setting, the derived CO diffusion barrier may instead be more representative of CO diffusion on H_2O ice surfaces, once all high-energy barrier CO-H_2O binding sites have been filled. The derived CO diffusion barrier of 170 K is a factor of 2–3 lower than what is currently assumed in astrochemical models also for surface diffusion. This implies that diffusion of CO, and other species, might be possible at much lower temperatures than currently assumed.

Chapter 6

Conclusions and future directions

6.1 Conclusions

The kinetics of CO diffusion into water ice at temperatures below its desorption were examined with a simple layering approach. This work provides an additional quantitative determination of the CO diffusion rate and barrier in amorphous water ice, which shows that the barrier is less than what is currently estimated in astrochemical models. Diffusion dependencies on temperature, ice thickness, porosity, and composition were explored. The main conclusions of these studies are the following:

1. CO is readily mobile in laboratory amorphous water even at temperatures as low as 15 K.

2. The rate of CO diffusion is directly correlated with the temperature of the ice environment.

3. The final fraction of mixed CO increases with the thickness of the water layer, but the rate is not affected by layer thickness.

4. The mechanism of the CO diffusion measured in these laboratory ices is a pore-mediated process, and is thought to be analogous to surface diffusion.

5. Exponential and Fickian analyses result in an energy barrier for CO diffusion in low-porosity amorphous water of ∼170 K, or 15 meV. This barrier value is potentially even lower in more porous or CO_2-contaminated water ices.

6.2 Future directions

Although the conclusions from this work, and other previous studies, have now indicated that the barrier value for CO diffusion in water ice is about 50% less than the lowest values used in current astrochemical models (Garrod 2013a), there are still several questions about the diffusion process left to be answered.

6.2.1 Understanding porosity effects and the coating hypothesis

Discussed in the previous chapter, the CO diffusion mechanism in lab-grown water ice may depend on the porosity of the water matrix. If the micropores have a wide enough pathway for several molecules of CO across, then it could be possible for the coating scenario proposed earlier to occur. Constraining whether or not the CO molecules are capable of coating, and then 'piggy-backing' on each other would be helpful for understanding the CO diffusion process both within water and on itself.

Several studies investigating the porosity of laboratory grown amorphous water ices (Kimmel et al. 2001; Raut et al. 2007) have shown that the ices become more porous with increasing angle of incidence during deposition with a collimated beam close to the sample substrates, similar to our setup. In these previous studies, the

lowest deposition temperature examined was 20 K, so it would be useful to perform similar experiments to measure the porosity fraction of ices deposited at several angles at temperatures as low as 12 K, or even lower. This would provide interesting information about the micropore sizes that are present in lab ice grown at temperatures where CO mixing can be observed. With that new information more experiments as an exte

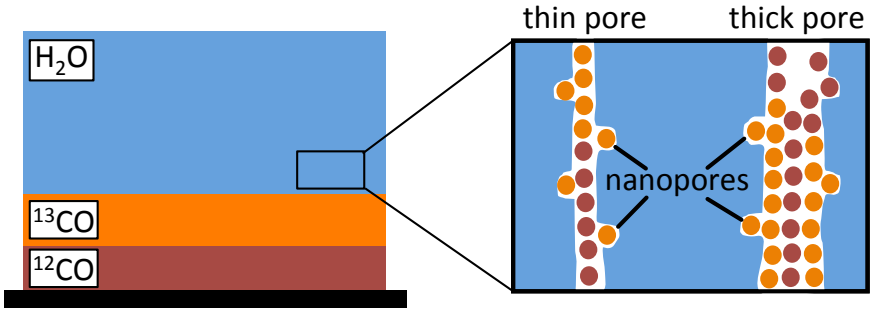

Fig. 6.1.— Schematic representing a proposed experiment to test the coating process concept. The film consists of water layered on top of two CO isotopologue layers. The CO isotopes may have different diffusion processes if the pores are thick or thin. ^{13}CO would diffuse to the top of the water layer first in thin pores, and in thick pores it would coat the lower part of the water layer, allowing the ^{12}CO to pass by and diffuse into the upper portion of the water layer.

Extensive porosity studies would be needed to test the coating process concept. Finding an angle of deposition that yields pores large enough would result in a different, most likely lower, energy barrier. Using layered CO isotopologues, see Fig. 6.2.1, could help distinguish if the pores are coated first, by monitoring the changes in the spectral features in each isotope band independently. If the changes occur at different times, or if the lower layer has negligible growth of the polar feature, that may indicate that coating of the surface is occurring. Desorption of CO could also be monitored in these experiments to give even more information. If the ice is subsequently heated to a temperature above the point of CO desorption, observing which isotope desorbed from the surface first would indicate the process by which the CO

diffused through the water layer. Although this experimental hypothesis is highly speculative, the results would be very interesting and could potentially lead to the measurement of CO diffusion on itself.

6.2.2 Bulk Diffusion

Conclusions from this and recent work indicate that the CO diffusion that measured in the laboratory thus far is during the movement along the pore wall surfaces, rather than within the bulk of the ice mantle. The strong binding nanopore sites may exhibit some similar properties to a site embedded within the mantle. Future experiments designed to isolate the process of CO diffusion out of a nanopore site could give insight into a bulk diffusion process. Karssemeijer et al. (2014) performed simulations that examined this process, and they concluded that 80 meV is required for CO to move out of a nanopore. Verifying the simulated value experimentally would be helpful, and would build upon our understanding of the ensemble of CO diffusion processes.

6.2.3 Other molecules

Quantitative experimental studies of diffusion processes in amorphous water ice are fairly recent, within the last several years. The choice to study CO diffusion was made because it is an important molecule for chemical processes happening on icy dust grains in cold interstellar regions. However, there are several more molecules that have been observed in interstellar ices, and their diffusion is also poorly understood. A next step for further studies involving other molecules would most likely be with CO_2, since it is also one of the next most abundant species observed. The experiments could be similar in nature to the ones performed in this work. Other less abundant species like methane, ammonia, and methanol could also be studied. Because these

molecules are larger than CO, there may be issues relating to pore size that should be considered when interpreting the data. This type of experimentation has potential to yield many important results about the diffusion properties of the species found in the ice mantles.

Chapter 7

Appendix

7.1 Chamber Procedures

1. Venting the chamber

   (a) Ensure cold cathode pressure gauge is OFF.

      i. With green light at the cold cathode position, press the "Sensor On/Off" button.

      ii. The green light will disappear and the reading says "OFF."

      iii. Leave the baratron and pirani gauges ON.

   (b) Ensure QMS is OFF.

      i. Pull power cord plug from the UPS box at the top of the racks. The QMS cord has white tape labeled "QMS."

      ii. The lights on the QMS unit will go off.

   (c) Ensure leak valve on the gas doser is in the closed position.

   (d) Close the green valve connecting the doser to the gas line.

i. Leave the gas line pump on.

(e) Close the black valve connecting the mechanical pump to the turbo pump.

i. Leave the mechanical pump on.

(f) Turn off differential pump at the back of the chamber.

(g) Turn off main turbo pump.

(h) Wait until the turbo and differential pumps completely slow to 0 Hz. (This typically takes about 1.5 hours)

(i) Ensure nitrogen is connected and flowing in the external gas line.

(j) Disconnect the external gas line from the chamber gas line.

(k) With nitrogen flowing, connect the external gas line to the vent port connection.

(l) Turn the sliver vent knob counter-clockwise slowly for several turns. The chamber pressure will slowly rise to atmospheric pressure.

(m) Stop the nitrogen flow after the chamber has reached atmospheric pressure.

(n) Close the vent valve.

(o) Disconnect the external gas line from the vent connection and reconnect to the chamber gas line.

2. Evacuating the chamber

(a) Ensure vent valve is closed.

(b) Open the black valve connecting the mechanical pump to the turbo pump.

i. Watch the baratron and pirani gauge readings decrease until they reach a stable value.

(c) Turn on differential pump at the back of the chamber.

i. Wait until it reaches 1500 Hz.

(d) Turn on main turbo pump.

i. Wait until it reaches 820 Hz.

(e) Wait for the chamber pirani gauge to read $\sim 5^{-3}$ Torr or lower.

(f) Turn on the cold cathode pressure gauge.

3. Cooling down the sample holder

(a) Turn the temperature controller box on.

(b) Press "SETPOINT" and then press "4" to set the temperature to 4 K.

(c) Turn on water faucet near helium compressor.

i. DO NOT adjust the black/gold valve, just turn on the water.

ii. Look at the flow meter to verify the water flow is 0.5–0.6 gal/min.

iii. Wait for a couple minutes to ensure water is flowing completely through the compressor.

(d) Check the resting pressure of the compressor.

i. The pressure should be 200–220 psi in the relaxed mode.

ii. If lower, add more He to the compressor.

A. Connect ultra-high purity (0.9999) He gas to the gas fill port.

B. Fill only to 200–220 psi, don?t overfill.

(e) Ensure the lights on the UPS for the compressor are on and green

(f) Turn on compressor

i. Listen for the pump to start cycling.

ii. Verify that the compressor pressure rises to 300 psi.

(g) Wait for temperatures to decrease to stable values.

i. Heater sensor typically gets to 4–5 K

ii. Sample sensor typically gets to 11 K

4. Using Temperature Controller

(a) A: Heater temperature reading

(b) B: Sample temperature reading

(c) 1: Setpoint temperature

(d) To set ramp rate

i. Press the ramp rate button (no. 6)

ii. Enter desired ramp rate using the number buttons

iii. Press "Enter"

(e) To set SETPOINT

i. Press "SETPOINT" button

ii. Enter desired setpoint temperature using the number buttons

iii. Press "Enter"

iv. The temperature will start to change at this point.

5. Evacuating the gas line

(a) Ensure the leak valve on the doser is in the closed position.

(b) Ensure all valves to canister, storage bulbs, lecture bottles, etc. are closed.

(c) Ensure green bar valve to pump line is closed.

(d) If not on already, turn on differential pump connected to the gas line; wait until it reaches 1500 Hz.

(e) If the line is at ATM pressure, slowly open valve to pump while monitoring the gas line pressure. BE CAREFUL not to open valve too much, or the pump will shut down.

References

Bacmann, A., Taquet, V., Faure, A., Kahane, C., & Ceccarelli, C. 2012, A&A, 541, L12

Bouwman, J., Ludwig, W., Awad, Z., et al. 2007, A&A, 476, 995

Chang, Q. & Herbst, E. 2012, ApJ, 759, 147

Chang, Q. & Herbst, E. submitted, ApJ

Escribano, R. M., Munoz Caro, G. M., Cruz-Diaz, G. A., Rodriguez-Lazcano, Y., & Mate, B. 2013, Proceedings of the National Academy of Science, 110, 12899

Garrod, R. T. 2013a, ApJ, 765, 60

Garrod, R. T. 2013b, ApJ, 778, 158

Garrod, R. T. & Herbst, E. 2006, A&A, 457, 927

Garrod, R. T. & Pauly, T. 2011, ApJ, 735, 15

Gerakines, P. A., Schutte, W. A., Greenberg, J. M., & van Dishoeck, E. F. 1995, A&A, 296, 810

Gibb, E. L., Whittet, D. C. B., Boogert, A. C. A., & Tielens, A. G. G. M. 2004, ApJS, 151, 35

Herbst, E. & van Dishoeck, E. F. 2009, ARA&A, 47, 427

Herbst, E. & Yates, Jr., J. T. 2013, Chemical Reviews, 113, 8707

Jenniskens, P. & Blake, D. F. 1994, Science, 265, 753

Karssemeijer, L. J., Ioppolo, S., van Hemert, M. C., et al. 2014, ApJ, 781, 16

Karssemeijer, L. J., Pederson, A., Jónsson, H., & Cuppen, H. M. 2012, Phys. Chem. Chem. Phys., 14, 10844

Katz, N., Furman, I., Biham, O., Pirronello, V., & Vidali, G. 1999, ApJ, 522, 305

Kimmel, G. A., Stevenson, K. P., Dohnálek, Z., Smith, R. S., & Kay, B. D. 2001, J. Chem. Phys., 114, 5284

Lauck, T. L., Karssemeijer, L. J., Shulenberger, K., et al. in prep, ApJ

Loeffler, M. J., Baratta, G. A., Palumbo, M. E., Strazzulla, G., & Baragiola, R. A. 2005, A&A, 435, 587

Mispelaer, F., Theulé, P., Aouididi, H., et al. 2013, A&A, 555, A13

Öberg, K. I., Boogert, A. C. A., Pontoppidan, K. M., et al. 2011, ApJ, 740, 109

Öberg, K. I., Bottinelli, S., Jørgensen, J. K., & van Dishoeck, E. F. 2010, ApJ, 716, 825

Öberg, K. I., Fayolle, E. C., Cuppen, H. M., van Dishoeck, E. F., & Linnartz, H. 2009, A&A, 505, 183

Öberg, K. I., Fraser, H. J., Boogert, A. C. A., et al. 2007, A&A, 462, 1187

Öberg, K. I., Lauck, T. N., & Graninger, D. submitted, ApJ

Pontoppidan, K. M., Boogert, A. C. A., Fraser, H. J., et al. 2008, ApJ, 678, 1005

Pontoppidan, K. M., Fraser, H. J., Dartois, E., et al. 2003, A&A, 408, 981

Raut, U., Famá, M., Teolis, B. D., & Baragiola, R. A. 2007, J. Chem. Phys., 127, 4713

Rowland, B., Fisher, M., & Devlin, J. P. 1991, J. Phys. Chem., 95, 1378

Sabri, T., Gavilan, L., Jäger, C., et al. 2014, ApJ, 780, 180

Sandford, S. A. & Allamandola, L. J. 1988, Icarus, 76, 201

Smith, R. S., Petrick, N. G., Kimmel, G. A., & Kay, B. D. 2011, Acc. Chem. Res., 45, 33

van Dishoeck, E. F., Herbst, E., & Neufeld, D. A. 2013, Chemical Reviews, 113, 9043

Venyaminov, S. & Prendergast, F. 1997, Ana. Biochem., 248, 234